PROCEEDINGS OF SCIENCE

Ultra-high-energy cosmic rays: propagation and detection

Denise Boncioli[*a,b], **Simone Rossoni**[c] **and Caterina Trimarelli**[a,b]
[a] *Dipartimento di Scienze Fisiche e Chimiche, Università degli Studi dell'Aquila via Vetoio, 67100, L'Aquila, Italy*
[b] *Istituto Nazionale di Fisica Nucleare, Laboratori Nazionali del Gran Sasso Assergi (AQ), Italy*
[c] *II. Institute for Theoretical Physics, Hamburg University, Luruper Chaussee 149, 22761, Hamburg, Germany*
E-mail: denise.boncioli@univaq.it, simone.rossoni@desy.de, caterina.trimarelli@aquila.infn.it

These notes comprise the topics covered at the first training school of COST Action CA18108 on "Quantum Gravity Phenomenology in the Multi-Messenger Approach" held in Corfu, Greece, from September 27th to October 5th 2021, regarding "Ultra-High-Energy Cosmic Rays: Propagation and Detection" and corresponding to four hours of lectures.

Corfu Summer Institute 2021 "School and Workshops on Elementary Particle Physics and Gravity" (CORFU2021)
29 August - 9 October 2021
Corfù, Greece

[*] Speaker.

PoS(CORFU2021)320

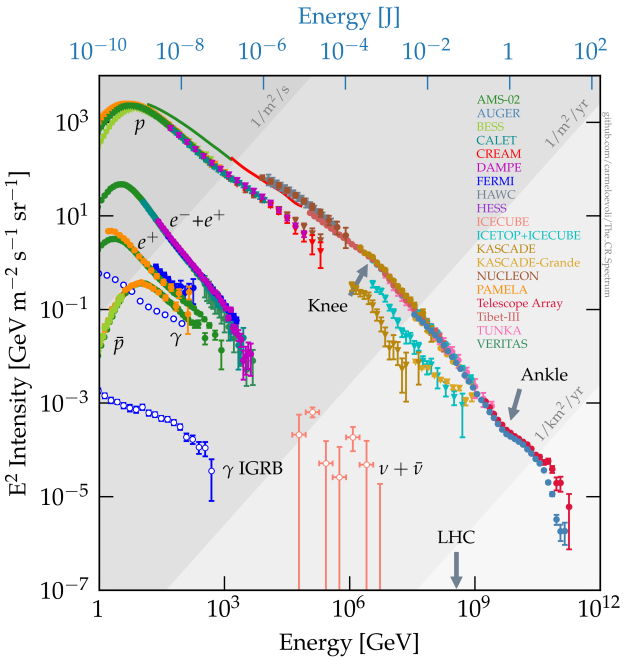

Figure 1: Global view of the cosmic-ray energy spectrum. From [1].

1. Introduction

At the beginning of the past century, a series of experiments realized by Domenico Pacini [2] and Victor F. Hess [3] revealed that a measured spontaneous "radiation" was coming from the outer space, and not from the Earth's crust. With forthcoming experiments, the nature of this radiation was established to be of particle nature, and we now know that *cosmic rays* are ionized nuclei, of which 90% are protons.

Cosmic rays are measured within a vast energy range; their energy density at Earth is recognized to follow a power law spectrum as $E^{-\gamma}$ with $\gamma \sim 3$ (see Fig. 1). In these lectures we are going to focus on the spectrum range at extremely high energies, namely above 10^{17} eV, where the cosmic rays are called Ultra-High-Energy Cosmic Rays (UHECRs). The particles' energy is here roughly more than eight orders of magnitude larger than the energy of a proton at rest, and the particles are therefore ultrarelativistic. Although theoretical studies and experimental efforts have been developed, several issues concerning UHECRs are still unsolved. The astrophysical origin of cosmic rays, as well as their chemical composition and the mechanisms that bring them to such extreme energies in their sites of production, are uncertain, and constitute a major and exciting field of study in astroparticle physics.

Due to the extreme high energy of UHECRs, and taking into account the confinement power of the magnetic fields in the Galaxy, we expect them not to be produced in the Galaxy. In order to estimate what type of extragalactic sources can host mechanisms to accelerate particles to such high energies, we can take inspiration from the acceleration mechanisms of particles in Supernova Remnants (SNRs). In these environments, the maximum energy reachable from particles due to the presence of shocks is connected to the age, and therefore to the dimension, of the SNR, as well

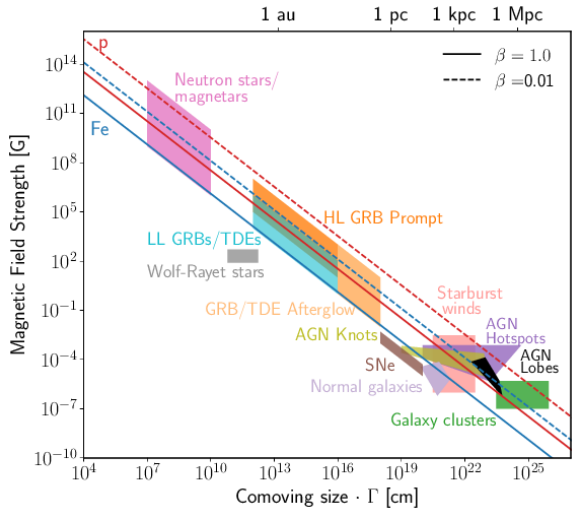

Figure 2: Source classes as a function of their comoving size and magnetic field, and corresponding maximum energy reachable for hydrogen and iron nuclei for different values of the shock velocity. Reproduced with permission from [7].

as to the intensity of the magnetic fields [4, 5]. This has been generalized in [6], and the maximum energy can be thus defined in terms of the confinement power of the astrophysical source, meaning that the particles can reside in the acceleration region as soon as the gyroradius is smaller than the region itself. This argument, known as "Hillas condition", permits to classify the candidate sources in terms of their comoving size and magnetic field in the acceleration region, as shown in Fig. 2, where the maximum energy is expressed as $E_{\rm max} = ZeBR$, being B the intensity of the magnetic field in the source, R the size of the accelerating region and Ze the charge of the particle. Several source types reported in Fig. 2 are capable to accelerate cosmic rays to ultra-high energies.
Some slight departures from a single power law in the CR spectrum can be recognized; for instance, a change of slope is visible at $\sim 3 \times 10^{15}$ eV, called *knee*. This could be interpreted as a signature of the end of the acceleration power of CR sources at work in the Galaxy, as due to processes in SNRs. Another change of slope, measured at $\sim 5 \times 10^{18}$ eV, called *ankle*, could be connected to the intersection of the spectra of Galactic and extragalactic CRs, as well as to different contributions from populations of extragalactic sources, or to effects of the energy losses of CRs during their travel through the extragalactic space. The origin of the suppression of the CR spectrum at the highest energies is also undetermined, as well as the other spectrum features. For a comprehensive and recent review of the open questions about cosmic rays, see Ref. [7].

The lecture notes are organized as follows. In Sec. 2 we introduce the physics of interactions that take place in the travel of the UHECR particles in the space they traverse before being detected, and the secondary particles that are expected to be produced in the propagation. In Sec. 3 we explain the characteristics of UHECR interactions in the Earth's atmosphere, and how they can be exploited in order to gather information about UHECRs. In particular, we also describe the largest UHECR observatory, the Pierre Auger Observatory, reporting the state-of-the-art of UHECR results in Sec. 4.

2. UHECR propagation

UHECRs traverse the extragalactic and Galactic space before being detected at Earth. Being the extragalactic space filled with photons with different wavelengths, UHECRs are expected to interact with them, possibly modifying their properties such as the initial energy and nuclear species they had at the escape from the source. Interactions in the Galaxy instead do not have a major impact on UHECRs. We therefore introduce the physics of the photo-hadronic interactions suffered by UHECRs; we discuss the expected features in the energy spectrum at Earth, as well as the characteristics of the fluxes of secondary particles generated in the propagation. The possible effects of the Galactic and extragalactic magnetic fields in the UHECR characteristics, including their arrival directions, will not be discussed in these notes; reviews about UHECR propagation in extragalactic magnetic fields can be found for instance in [8, 9].

2.1 UHECR interactions with photon backgrounds and expected fluxes at Earth: the case of protons

In this section we introduce the computation of the interaction rate, which will be used in the calculation of the expected flux at Earth, in the case of CR protons. The relevant photon fields for the interactions of the UHECRs are mainly the Cosmic Microwave Background (CMB) and the ultraviolet to optical to infrared background light (also called Extragalactic Background light, EBL). Among the photo-nuclear interactions, the photo-disintegration of UHECR nuclei heavier than hydrogen and the photo-meson production have to be considered. In addition, the production of pairs of electrons and positrons has to be taken into account among energy losses.

The final goal of this lecture is to provide a procedure to calculate the expected UHECR flux at Earth. As a first step, we evaluate the energy losses due to the interactions; due to the relativistic energies of the involved particles, in order to describe a process such as $a+b \to c+d$, where a, b, c, d are the particles in the initial and final states, we define their energy-momentum four-vectors as

$$(E_i, \vec{p}_i) \tag{2.1}$$

and compute the s of the process, namely the scalar product of the cumulative four-vectors of the initial and final states, that is a Lorentz invariant quantity. As a general approach applied to any of the processes described in the following, the value of $s_{\rm th}$, namely the s at the threshold for the reaction, will be computed in a convenient reference frame, such as

$$s_{\rm th} = (E_a + E_b)^2 - (\vec{p}_a + \vec{p}_b)^2 = (m_c^2 + m_d^2), \tag{2.2}$$

corresponding to the laboratory frame. This quantity will be calculated corresponding to the interactions relevant in the propagation of the particles through the extragalactic space.

Already at the time of the discovery of the CMB, it was supposed that the photo-pion production $p + \gamma_{\rm bkg} \to p(n) + \pi^0(\pi^+)$ of protons off CMB photons could cause energy losses inducing a suppression of the UHECR flux [10, 11]. The threshold for this process can be calculated as:

$$s_{\rm th} = m_{\rm p}^2 + 2E_{\rm th}\varepsilon(1 - \beta\cos\theta) = (m_{\rm p} + m_\pi)^2 \tag{2.3}$$

where $m_{\rm p}, m_\pi$ are the proton and the pion mass, respectively, β is the speed of the proton in the laboratory frame (being the particles ultrarelativistic, this can be taken as $\beta \sim 1$ and will be omitted

in the following), θ is the angle between the photon and the proton momenta, ε is the energy of the photon in the laboratory frame and $E_{\rm th}$ is the minimum energy required for the proton in order to induce a pion production, which reads:

$$E^{\pi}_{\rm th,p} = \frac{m_\pi^2 + 2 m_\pi m_{\rm p}}{2\varepsilon(1-\cos\theta)} \approx 7\times10^{19}\,{\rm eV} \tag{2.4}$$

if head-on collisions are taken into account with a photon of $\varepsilon \approx 7\times10^{-4}\,$eV (average CMB photon energy).

Another process that can cause energy losses of CR protons is the electron-positron pair production, $p+\gamma_{\rm bkg} \to p + e^+ + e^-$, for which the energy threshold can be calculated similarly to the pion production case:

$$E^{e^+e^-}_{\rm th,p} = \frac{4m_{\rm e}^2 + 8 m_{\rm e} m_{\rm p}}{2\varepsilon(1-\cos\theta)} \approx 6\times10^{17}\,{\rm eV}\,. \tag{2.5}$$

In order to evaluate what photon fields can play a role in these processes, one can compute the energy of the photon in the proton rest frame: $\varepsilon' = \varepsilon\Gamma(1-\cos\theta) \approx \varepsilon\Gamma$ (here and in the following the primed terms refer to the quantities computed in the proton/nucleus rest frame). Therefore the needed threshold Lorentz factor to trigger a photo-pion reaction in the EBL (mean infrared energy $10^{-1} \div 10^{-2}$ eV) will be lower than what is found for the CMB photons, also permitting lower energy protons to induce the production of pions. Although the pion production by protons off EBL is less efficient in terms of energy losses if compared to the pair production in the same energy range, this is relevant in terms of production of neutrinos (as discussed in Sec. 2.3).

The typical time of an interaction process is approximately proportional to $1/(c\sigma n_\gamma)$, where σ represents the cross section of the process, while n_γ is the density of the photons encountered by the cosmic ray in the extragalactic space. If the distribution of these quantities in terms of energies is considered, the interaction rate can be computed as reported in App. A, finding:

$$\frac{dN_{\rm int}}{dt} = \frac{c}{2\Gamma^2}\int_{\varepsilon'_{\rm th}}^{\infty}\sigma(\varepsilon')\varepsilon'\int_{\varepsilon'/2\Gamma}^{\infty}\frac{n_\gamma(\varepsilon)}{\varepsilon^2}d\varepsilon d\varepsilon'\,. \tag{2.6}$$

Here σ is the cross section of the considered process and n_γ is the energy spectrum of the photon field, as a function of the energy of the photon in the proton rest frame and as a function of the energy of the photon in the laboratory frame, respectively. If the energy spectrum of CMB photons (black body)

$$n_\gamma = \frac{dN_\gamma}{dV d\varepsilon} = \frac{1}{\pi^2(\hbar c)^3}\frac{\varepsilon^2}{\exp(\varepsilon/k_{\rm B}T)-1} \tag{2.7}$$

is considered (where we also assume isotropy, so that $n_\gamma(\varepsilon,\cos\theta) \approx n_\gamma(\varepsilon)$), the calculation of the integral over the photon density can be worked out analytically [12], with the transformation $y = \exp(\varepsilon/k_{\rm B}T)-1$. The interaction rate becomes then

$$\frac{dN_{\rm int}}{dt} = \frac{ck_{\rm B}T}{2\pi^2(\hbar c)^3\Gamma^2}\int_{\varepsilon'_{\rm th}}^{\infty}\sigma(\varepsilon')\varepsilon'\left\{-\ln\left[1-\exp\left(-\frac{\varepsilon'}{2\Gamma k_{\rm B}T}\right)\right]\right\}d\varepsilon'\,. \tag{2.8}$$

In order to compute the energy loss length, the inelasticity of the processes taken into account has to be evaluated, meaning the mean fraction of energy of a nucleus lost in a single interaction,

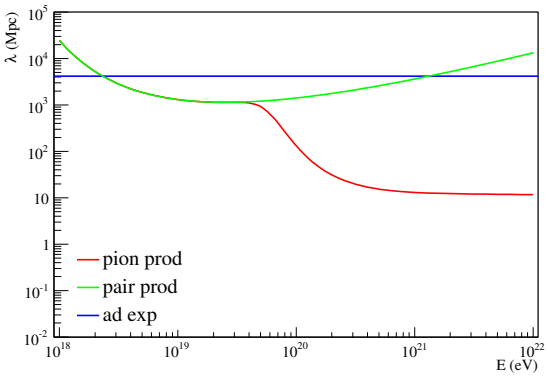

Figure 3: Total energy loss length for protons in the CMB as a function of the energy, calculated at redshift $z = 0$. The red line representing the pion-production length is only shown down to the pair production length. From [14].

$f(\varepsilon') = \langle \frac{E_{\rm in} - E_{\rm out}}{E_{\rm in}} \rangle$. The inelasticity at the threshold for the production can be computed taking into account the masses of the particles to be generated, so that $f_\pi(\varepsilon' \approx 145\,{\rm MeV}) = \frac{m_{\pi^0}}{m_{\rm p}+m_{\pi^0}} \approx 0.125$ and $f_{e^+e^-}(\varepsilon' \approx 1\,{\rm MeV}) = \frac{2m_{\rm e}}{m_{\rm p}+2m_{\rm e}} \approx 10^{-3}$ corresponding to photo-pion and pair production respectively. In order to compute the same quantities at energies higher than the threshold, the particle distributions in the final states are needed. In the energy range of interest for CR interactions, the inelasticity is approximated as 20% for the photo-pion production and 10^{-5} for the pair production [13].

The interaction length in Eq. 2.6 can be used to compute the energy loss rate, by introducing the inelasticity, as:

$$\frac{1}{E}\frac{dE}{dt} = -\frac{c}{2\Gamma^2}\int_{\varepsilon'_{\rm th}}^{\infty} f(\varepsilon')\sigma(\varepsilon')\varepsilon' \int_{\varepsilon'/2\Gamma}^{\infty} \frac{n_\gamma(\varepsilon)}{\varepsilon^2} d\varepsilon d\varepsilon' \,, \tag{2.9}$$

for a generic process. This rate can be thus converted into a length as:

$$l_{\rm loss} = -c\left(\frac{1}{E}\frac{dE}{dt}\right)^{-1} = -E\frac{dx}{dE} \tag{2.10}$$

and used to follow the trajectory of the particle as

$$\frac{dE}{dx} = -\frac{E}{l_{\rm loss}} \tag{2.11}$$

being x the distance covered by the particle. Fig. 3 shows the energy loss lengths corresponding to different processes for protons in the CMB, as a function of the energy. The horizontal line shows the adiabatic energy losses due to the expansion of the Universe, that are given by:

$$\frac{1}{E}\frac{dE}{dt} = -H(z)\,, \tag{2.12}$$

where $H(z) = H_0\sqrt{(1+z)^3\Omega_m + \Omega_\Lambda}$ (see also App. B and **??**). At intermediate energies the effect of the energy losses due to the pair production is dominant; the typical length traversed by CRs

undergoing these processes is of the order of Gpc. At the highest energies photo-pion processes can take place, and the typical length is of the order of 10 Mpc. This means that if CRs with EeV energies are detected at Earth, these should be produced within a sphere of the order of $\sim$ 100 Mpc, as predicted by [10, 11].

The energy loss lengths in Fig. 3 are computed corresponding to the present time (or redshift, as defined in App. B). Due to the dependence of the density of the CMB photons on the redshift and the dependence of the temperature of the CMB photons, the energy loss length varies as:

$$l_{\rm loss}(E,z) = \frac{l_{\rm loss}((1+z)E, z=0)}{(1+z)^3}\,, \tag{2.13}$$

while if the EBL is used instead of the CMB, the expression above has a more complicate dependence on z. The complete computation of Eq. 2.13 is reported in App. C.

2.1.1 Expected UHECR fluxes

The expected number of particles at Earth per unit energy, time and area can be computed, considering a uniform distribution of identical sources in the Universe, as

$$\frac{dN_{\rm obs}}{dE\,dt\,dA} = \int \frac{dN_{\rm src}}{dE_{\rm src}\,dt_{\rm src}} \frac{dn_{\rm src}}{dV} \left(\frac{\partial E_{\rm src}}{\partial E}\right) \frac{1}{4\pi R^2} R^2 dR d\Omega\,. \tag{2.14}$$

The first term in Eq. 2.14 represents the number of particles ejected from the source per unit energy and time $Q(E_{\rm src}) = \frac{dN_{\rm src}}{dE_{\rm src}dt_{\rm src}}$, from which the luminosity in cosmic rays can be derived as

$$L_{\rm src} = \int E_{\rm src}\, Q(E_{\rm src})\, dE_{\rm src}\,. \tag{2.15}$$

Taking into account the acceleration processes in the source environment, the spectrum at the source can be written as

$$Q(E_{\rm src}) = Q_0 \left(\frac{E_{\rm src}}{E_0}\right)^{-\gamma} f_{\rm cut}(E_{\rm src})\,, \tag{2.16}$$

being γ the spectral index and $f_{\rm cut}(E_{\rm src})$ a function that describes the cut-off of the flux at the source, which might depend on the acceleration process and/or the interactions suffered by the particles in the source environment. The normalization Q_0 (and thus also the luminosity $L_{\rm src}$ in Eq. 2.15) can be derived if the expected flux is compared to the experimental data. The value of E_0 can be taken as 10^{18} eV.

Being the sources located at cosmological distances, we have to use the transformation $R = cdt = \eta(z)dz$ (as defined in App. B), thus obtaining:

$$\frac{dN_{\rm obs}}{dE\,dt\,dA\,d\Omega} = \int \frac{dN_{\rm src}}{dE_{\rm src}\,dt_{\rm src}} \frac{dn_{\rm src}}{dV} \left(\frac{\partial E_{\rm src}}{\partial E}\right) \eta(z) dz\,. \tag{2.17}$$

The Jacobian term $\left(\frac{\partial E_{\rm src}}{\partial E}\right)$ reported in Eq. 2.14 and 2.17 is connected to the calculations of the variation of the energy as a function of the time (or the redshift) in Sec. 2.1, being

$$E_{\rm src}(E,t) = E + \int_t^{t_0} dt \left[\left(\frac{dE}{dt}\right)_{\rm ad} + \left(\frac{dE}{dt}\right)_{\rm int}\right], \tag{2.18}$$

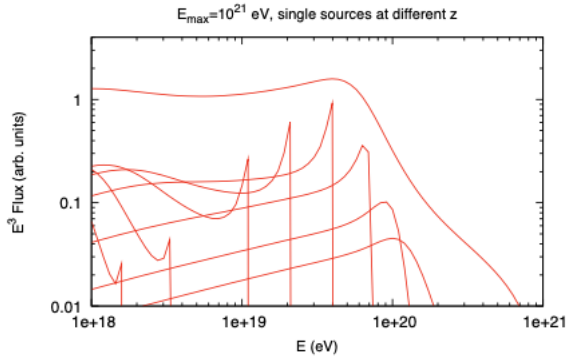

Figure 4: Expected flux of cosmic-ray protons at Earth, multiplied by E^3, corresponding to protons injected with a power law with $\gamma = 2.6$ and maximum acceleration energy at the source $E_{\rm cut,src} = 10^{21}$ eV (indicated as $E_{\rm max}$ in the top of the figure), from a uniform distribution of identical sources (upper line). Expected fluxes from single sources are also shown, with redshift respectively (with decreasing energy cutoff): 0.005 ($\sim$20 Mpc), 0.01 ($\sim$ 40 Mpc), 0.03 ($\sim$125 Mpc), 0.1 ($\sim$420 Mpc), 0.2 ($\sim$820 Mpc), 0.3 ($\sim$1200 Mpc), 0.5 ($\sim$1890 Mpc), 0.7 ($\sim$2500 Mpc), 0.9 ($\sim$3000 Mpc). From [14].

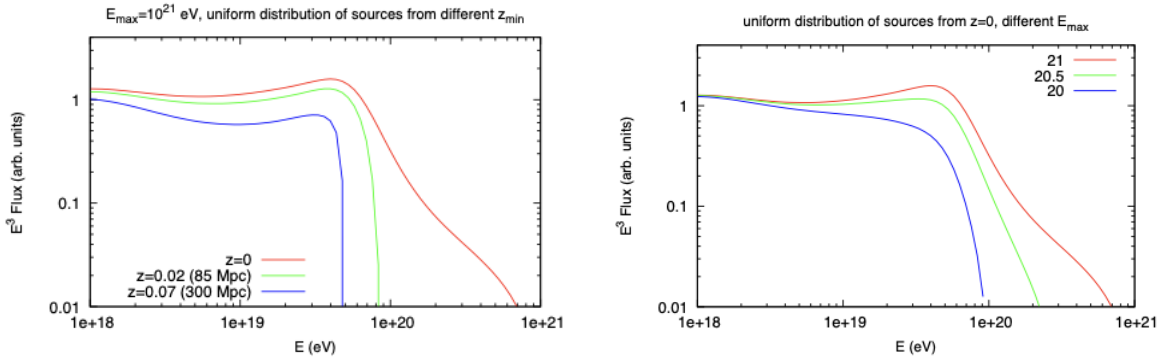

Figure 5: Expected flux of cosmic-ray protons at Earth, multiplied by E^3, corresponding to protons injected with a power law with $\gamma = 2.6$ and maximum acceleration energy at the source $E_{\rm cut,src} = 10^{21}$ eV (indicated as $E_{\rm max}$ in the top of the figure), from a uniform distribution of identical sources. Left: $E_{\rm cut,src} = 10^{21}$ eV at injection, uniform distribution of sources starting from different $z_{\rm min}$. Right: $E_{\rm cut,src}$ (indicated as $E_{\rm max}$ in the top of the figure) variable, uniform distribution of sources starting from $z_{\rm min} = 0$. From [14].

where both the contributions the energy losses from the adiabatic expansion of the Universe and the interactions are included. The Jacobian term can be written as (the complete derivation can be found in App. D):

$$\frac{dE_{\rm src}(E,t)}{dE} = \frac{dE_{\rm src}(E,t)}{dt}\left(\frac{dE}{dt}\right)^{-1} . \tag{2.19}$$

We can therefore compute the expected flux of UHECR protons at Earth as in Eq. 2.17, corresponding to an expanding universe homogeneously filled by sources of accelerated primary UHE protons with some choice for the spectrum at the source reported in Eq. 2.16. An example is reported in Fig. 4, where the contribution of single sources at different distances and the cumulative

spectrum (multiplied by E^3) are depicted, corresponding to $\gamma = 2.6$ and $E_{\rm cut} = 10^{21}$ eV, being defined as $f_{\rm cut}(E_{\rm src}) = \exp(-E_{\rm src}/E_{\rm cut,src})$. The closest sources show no deviations from the initial spectrum, while corresponding to increasing distances a bump is visible, as expected due to the rapid pile-up of the protons below the photo-pion threshold [16]. The abrupt suppression of the individual spectra, which is also reflected in the diffuse spectrum at the highest energies, is the effect of the energy losses due to photo-pion processes, as predicted in [10, 11], commonly known as "GZK" suppression from the initials of the authors. The bump is then expected to be smoother in the diffuse flux, because individual peaks are located at different energies. Below the bump, a dip is visible at larger distances, as expected due to the pair production energy losses [17]. In the diffuse flux the protons in the dip should be collected from a large volume, thus one could expect this feature to be less dependent on the distribution of sources. The measured change of the slope at 5×10^{18} eV, the ankle, could therefore, in the context of pure proton composition of UHECRs, be interpreted as a signature of the propagation of the protons through the CMB.
Attributing the suppression of the spectrum to the GZK effect is however not entirely justified. In fact, at the highest energies the visible Universe in terms of cosmic rays is strongly dependent on the local distribution of sources. As an example, in Fig. 5 (left panel) we show the change in the suppression at the highest energies as due to the redshift of the closest source: the farther is the closest source, the lower is the energy of the suppression. A similar effect can be obtained if the maximum energy at the acceleration is varied (see Fig. 5, right panel), indicating that the shape of the suppression is degenerate in terms of these variations, which would contribute to the depletion of the flux as well as the "pure" GZK effect.

By comparing the experimental spectrum at Earth with the expected one, it is in principle possible to attribute the features of the observed spectrum to the effects of the interactions suffered by protons in the extragalactic propagation, and to the characteristics of the spectrum at the escape from the sources, in terms of the spectral index and of the maximum energy in Eq. 2.16. An example of a fitting procedure for obtaining the best reproduction of the experimental spectrum is given in [18]. For the case of a pure proton composition at the source, and assuming a homogeneous distribution of identical sources with injection:

$$J(E) \propto S(z) \left(\frac{E_{\rm src}}{E_0}\right)^{-\gamma} \exp(-E_{\rm src}/E_{\rm cut,src}) \,, \tag{2.20}$$

being $S(z) \propto (1+z)^m S_{\rm SFR}(z)$ (where $S_{\rm SFR}(z)$ is the source evolution corresponding to the star forming rate as given in [19]), the data are best reproduced corresponding to $(\gamma, E_{\rm cut,src}, m) = (1.52, 19.7, 4.3)$. Such values are further constrained when the corresponding fluxes of the neutrinos produced during the UHECR propagation in the extragalactic space are compared to the current experimental limits, as done in [18].

2.2 UHECR interactions with photon backgrounds and expected fluxes at Earth: the case of nuclei

Current measurements of the cosmic rays at the highest energies are found to be inconsistent with a pure-proton composition, using current hadronic interaction models for taking into account

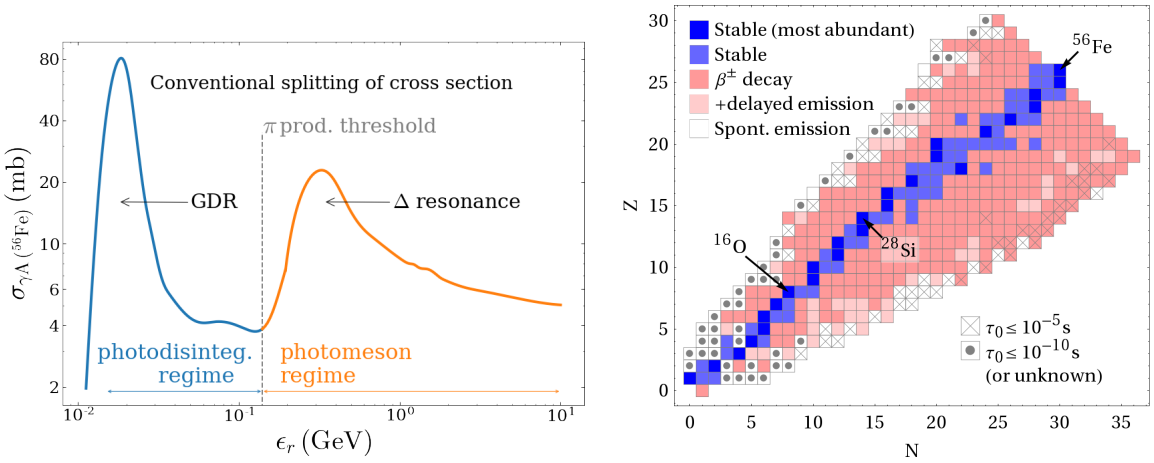

Figure 6: Left: Total inelastic photonuclear cross section for iron-56 as a function of photon energy in the nucleus' rest frame. Reproduced with permission from [23]. Right: Nuclear chart as a function of the number of protons and neutrons, showing the isotopes that can be created in the cascade after the first interaction of an isotope of iron-56 with a background photon. Reproduced with permission from [24].

the development of the cascade of particles generated in the atmosphere after the first interaction of the primary cosmic ray [20, 21].

If cosmic rays reaching the top of the atmosphere are heavier than protons, their possible interactions must be taken into account for the propagation through extragalactic photons in order to possibly infer the UHECR mass composition and spectral parameters at their sources. In addition to the electron-positron pair production and the photo-pion production, the photo-disintegration process plays an important role in the modification of the nuclear species of the cosmic rays as escaped from their sources, on their way to the Earth. Unlike the pion production, the disintegration of nuclei can be triggered correspondingly to energies of the photon in the nucleus rest frame of tens of MeV. At these energies it is possible to neglect the binding energy of the nucleons in the nucleus, therefore the energy loss lengths can be computed as separated contributions from the modification of the Lorentz factor (due to energy losses from adiabatic expansion, pair production and pion production) and the change in the atomic mass number, due to the photo-disintegration, where the Lorentz factor is conserved:

$$\frac{1}{E}\frac{dE}{dt} = \frac{1}{\Gamma}\frac{d\Gamma}{dt} + \frac{1}{A}\frac{dA}{dt}\,. \tag{2.21}$$

The photo-disintegration process comprises two main regimes [22, 14], as shown in Fig. 6 (left):

- a resonance at about 10 MeV (energy of the photon in the nucleus rest frame, slightly dependent on the nucleus), called Giant Dipole Resonance (GDR), corresponding to the behavior of protons and neutrons in the nucleus as penetrating fluids; the de-excitation of this resonance produces the ejection of one or two nucleons;

- a flat region in the range 20 - 150 MeV, where the photon wavelength in the nucleus rest frame is comparable to the nuclear dimensions and the photon is likely to interact with a nucleon pair, with the final ejection of that pair and possibly other nucleons.

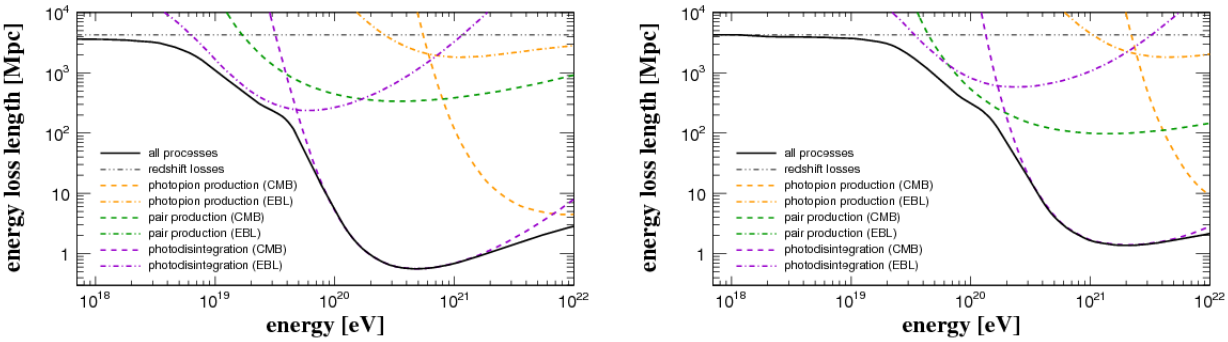

Figure 7: Energy loss lengths for nitrogen-14 (left) and iron-56 (right), calculated at $z = 0$. Reproduced with permission from [29].

The disintegration of nuclei and the consequent production of lighter fragments originate a cascade of nuclear reactions that would not be present in case of a pure proton composition (see Fig. 6, right, for the case of a cascade initiated by an iron-56), and impose a more complex treatment of the computation of the extragalactic propagation. Several codes have been implemented to treat these interactions, with different approaches, such as the ones in [12, 25, 26, 27]. In particular, in [12, 25] the analytic calculations of the expected spectra of cosmic ray nuclei at Earth are worked out, for the case of CMB and EBL respectively.

Examples of energy loss lengths are shown in Fig. 7, corresponding to nitrogen (left) and iron (right) nuclei. Similarly to the case of protons, the adiabatic energy losses are dominant at low energies. At intermediate energies, the pair production is overcome by the photo-disintegration on the EBL, while at the highest energies the dominant process is the photo-disintegration on the CMB. The pion production is shifted towards higher energies with respect to the case of protons. This is due to the fact that in this process the particle involved is the nucleon in the nucleus, therefore the threshold is $E_{\rm th} \approx A\Gamma^p_{\rm th} m_p c^2$, where $\Gamma^p_{\rm th}$ can be derived from Eq. 2.4. Therefore, the pion production will be more efficient in the case of protons with respect to heavier nuclear species, and this will have consequences for the production of secondary messengers (see Sec. 2.3).

It is interesting to note here that similarly to the pion production for protons, also the photo-disintegration entails the disappearance of nuclei of a certain species, because of the creation of lighter fragments, and the excitation of the GDR for the interactions with CMB photons happens at similar energies as for the threshold of the pion production of protons on CMB. In addition, the energy loss lengths for the photo-disintegration processes are of similar order of magnitude as the one for the pion production from protons. For these reasons, the visible Universe in terms of cosmic rays at the highest energies is similar for protons and heavy nuclei (as one can see in Fig. 8, where simulations of *SimProp* 2.4 [27] are used to show the energy at Earth as a function of the distance of the source that produced a cosmic ray particle of the species indicated in the legend). This implies that the interpretation of the suppression of the spectrum, experimentally observed at the highest energies, is also degenerate in terms of the chemical composition of the cosmic rays, in addition to the other possible motivations due to the pion production effect (if protons), the distribution of the sources and the maximum energy at the acceleration. Understanding the origin of the suppression of the spectrum, as well as of its other features, requires considering other CR observables such as

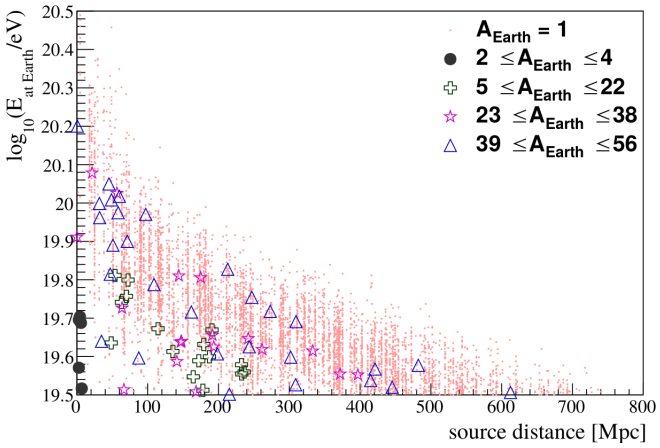

Figure 8: Energy at Earth as a function of the distance at which the cosmic ray is created, for different nuclear species, computed from a *SimProp* 2.4 [27] simulation. Courtesy of A. di Matteo [28].

the ones connected to the chemical composition, as proposed for instance in [30], and constitutes one of the main open issues in cosmic-ray astrophysics.

2.3 Secondary messengers

The interactions suffered by cosmic ray particles during their passage through CMB and EBL generate secondary particles that in turn decay. The photo-pion processes involve the excitation of the Delta resonance, whose de-excitation can produce charged or neutral pions, that in turn decay and produce neutrinos or gamma-rays, called *cosmogenic*.

Let us first discuss the case of the production of charged pions as:

$$\begin{aligned} p + \gamma_{\text{bkg}} \to \Delta^+ \to \pi^+ + n \\ \pi^+ \to \mu^+ + \nu_\mu \\ \mu^+ \to e^+ + \nu_e + \bar{\nu}_\mu \end{aligned} \tag{2.22}$$

Therefore three neutrinos (with flavor composition of $\nu_e : \nu_\mu : \nu_\tau = 1 : 2 : 0$) for each pion are produced. From considerations about the inelasticity, as reported in Sec. 2.1, the pions carry 20% of the energy of the primary proton. The expected flux of cosmogenic neutrinos at Earth depends on the characteristics of the spectrum of protons emitted from the sources. From Eq. 2.22 one can see that the expected fluxes of electron/ muon neutrinos and muon anti-neutrinos (reported in Fig. 9, right panel) are expected to be of equal intensity (they are produced for each $p\gamma$ interaction), and peaked at the same energy (they carry on average 5% of the energy of the initial proton). A contribution of electron anti-neutrinos can arise from the decay of neutrons, and its flux is expected to be peaked at lower energies. Anti-electron neutrinos which can be produced from the decay chain of negative pions (possibly produced in multi-pion productions) can also contribute to the high-energy neutrino peak (see Fig. 9, left panel).

The expected neutrino flux is also connected to the photon fields with which the protons can interact. In order to trigger a photo-pion production off a CMB photon (average energy $\varepsilon \approx 7 \cdot 10^{-4}$

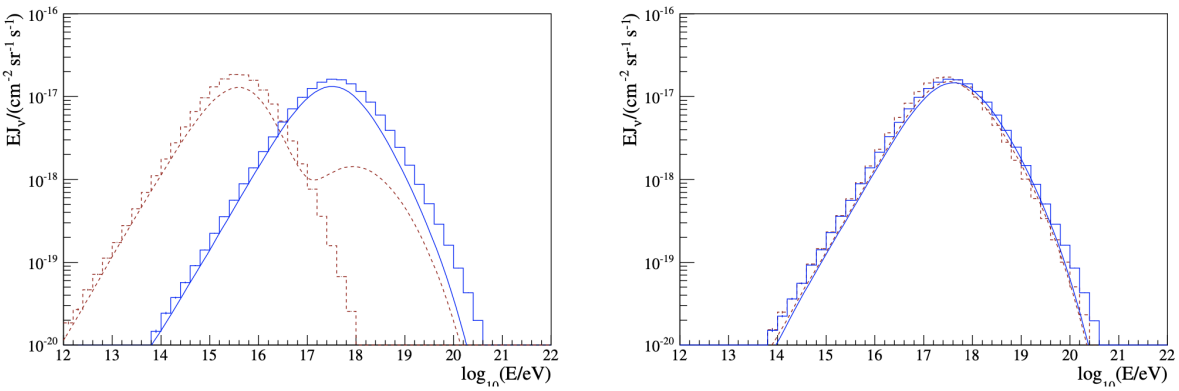

Figure 9: Left panel: fluxes of electron (blue solid) and anti-electron (red dashed) neutrinos generated in propagation of protons through CMB. Right panel: fluxes of muon (blue solid) and anti-muon (red dashed) neutrinos. The histograms are obtained from SimProp simulations, while the lines are taken from [31]. Reproduced with permission from [32].

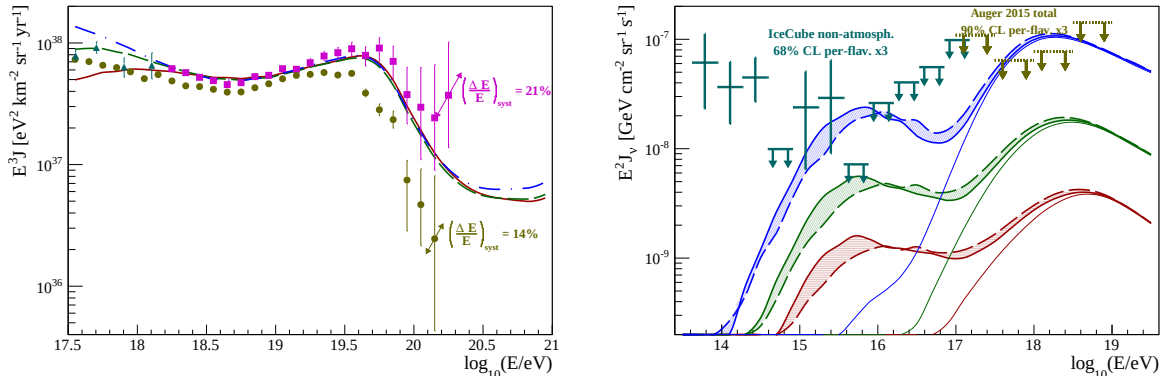

Figure 10: Left panel: cosmic-ray fluxes expected at Earth (in this case, the propagation through both CMB and EBL is computed) in scenarios with pure proton composition, with various models for the cosmological evolution of sources (solid red: no evolution; dashed green: SFR evolution [19]; dot-dashed blue: AGN evolution [33]). For comparison also the experimental data from the Telescope Array [34] and the Pierre Auger Observatory [35] are shown (magenta and olive green dots, respectively). Right panel: fluxes of neutrinos in the same scenarios. Reproduced with permission from [32].

eV), a more energetic proton with respect to the case of the EBL field is needed, being the energy of the photon in the nucleus rest frame $\varepsilon' \approx \Gamma\varepsilon$. As a consequence, the high energy peak of the neutrino flux is expected to be originated from interactions off CMB, while the low energy peak from interactions off EBL.

Neutrinos can travel for long distances unimpeded; this is the reason why they can be accumulated for a large portion of the Universe, as can be seen in the different colors of the lines in Fig. 10 (right panel). Here the cases of no cosmological evolution of the distribution of UHECR sources is reported (red line) together with the case of SFR evolution (green line) [19] and the case of evolution of the high-luminosity Active Galactic Nuclei (AGN) as suggested in [33]. The effect

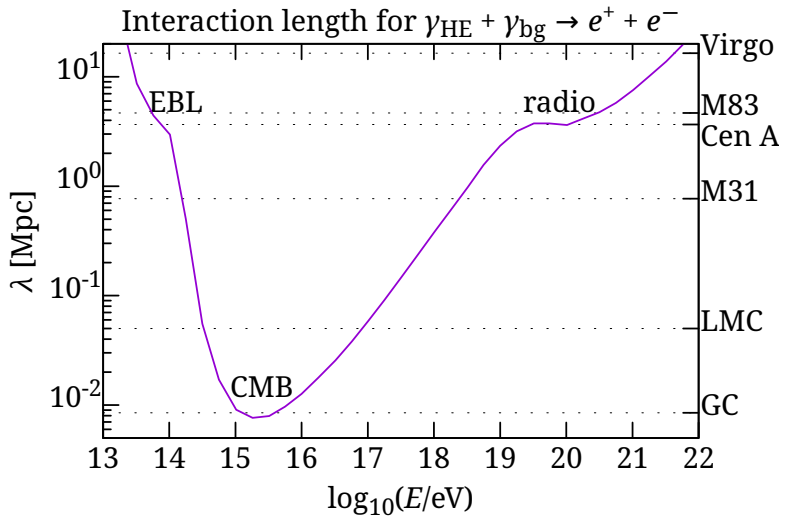

Figure 11: Interaction length of gamma rays for pair production in several background fields. Courtesy of A. di Matteo.

of the cosmological evolution, to be considered in Eq. 2.17 as a term like $(1+z)^m$ entering in the distribution of sources, is expected to be more important while increasing the redshift. Due to the interactions of UHECR particles, the effect of the cosmological evolution of sources is less dominant than for neutrinos, as can be seen in the left panel of Fig. 10, where the spectra are different only below $10^{18.2}$ eV.

Combining the information from UHECRs and neutrinos can be, therefore, very relevant to the aim of constraining the cosmological distribution of the sources, which remains undetermined if only UHECRs are taken into account. Examples of combined studies involving both the UHECR spectrum (with pure proton composition) and the expected cosmogenic neutrinos can be found for instance in [18, 36]. The expected flux of cosmogenic neutrinos is strongly related to the characteristics of the flux of UHECRs at the escape from the sources, as well as from the details of the cosmological evolution of UHECR sources. The maximum energy of UHECRs determines the cutoff of the neutrino flux, while the shape of the neutrino flux is mainly dependent on the spectral index of the UHECR spectrum. The chemical composition of UHECRs is affecting the expected neutrino flux; due to the fact that the photo-pion production is a process involving the nucleons in the nucleus, it is convenient to compute the value of the threshold Lorentz factor, which for the photo-pion production reads $\Gamma_{\rm th} \approx 7 \times 10^{10}$. Therefore the energy threshold for a photo-pion process for a generic nucleus is $E_{\rm th} = A\Gamma^p_{\rm th} m_p c^2$; nuclei heavier than hydrogen would then require A times the energy of a proton in order to excite the resonance responsible for this process. For this reason, scenarios involving heavier nuclear composition of UHECRs predict a smaller neutrino flux [37, 38].

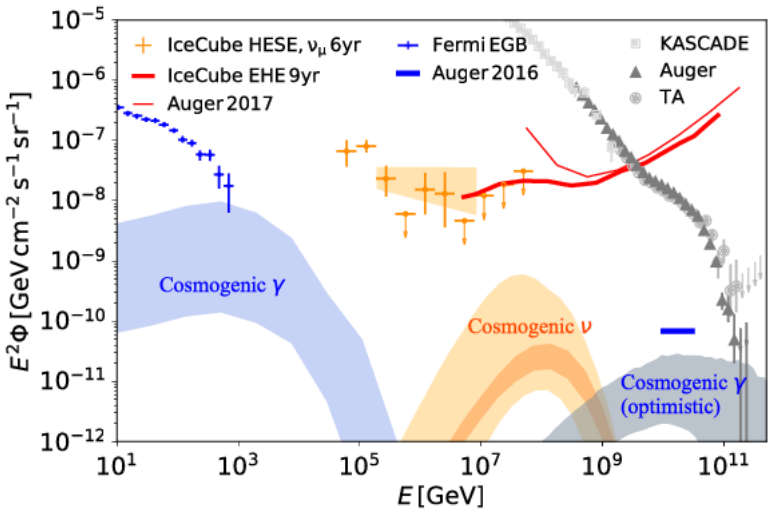

Figure 12: Cosmogenic photon (blue) and neutrino (orange) fluxes for UHECR models that fit the Pierre Auger Observatory data including spectrum and composition. Reproduced with permission from [7].

Neutral pions can be produced in the de-excitation of Δ^+, giving origin to cosmogenic photons:

$$\begin{aligned} p + \gamma_{\rm bkg} \to \Delta^+ \to & \pi^0 + p \\ & \pi^0 \to \gamma + \gamma \end{aligned} \tag{2.23}$$

Similarly to cosmic rays, cosmogenic photons can interact with photon backgrounds (interaction lengths for these processes are shown in Fig. 11), giving rise to electromagnetic cascades, where in turn high energy photons can be absorbed due to pair production, and electrons undergo inverse Compton and produce synchrotron radiation, transferring energy to the range below 10^{14} eV.

It is interesting to notice that the energy densities in UHECRs, high-energy neutrinos and gamma-rays are similar (as reported in Fig. 12). This would suggest that the origin of these different messengers is strongly connected and support a multi-messenger view, which might strongly improve our understanding of the characteristics of UHECRs and other messengers.

2.4 Quantum gravity signals in UHECR propagation

Due to the extreme energies of UHECRs, it is possible to test the validity of the Lorentz invariance by searching for effects in the propagation of UHECRs through the extragalactic space. This can be done with a phenomenological approach, changing the energy dispersion relation as:

$$E_i^2 - p_i^2 = m_i^2 + \sum_{n=0}^{N} \delta_{i,n} E_i^{2+n}, \tag{2.24}$$

depending on the order n of the perturbation; the parameters of the violation can also be written in terms of the Planck mass. As an example, due to the violation, the energy threshold of the photopion production for protons as well as the typical energies for the photodisintegration of nuclei might be shifted to very large energies so that they are in reality inhibited. For this reason, the

suppression of the flux because of energy losses due, for instance, to the photo-pion processes, is not expected in the flux at Earth if Lorentz invariance violation (LIV) exists [40]. Therefore, the experimental evidence of the suppression of the UHECR flux at the highest energies [41] can be exploited in order to constrain LIV parameters, as done in [42, 43, 44, 45].

Other approaches for testing LIV with UHECRs and multi-messenger studies in general can be found in [46].

3. UHECR detection

The detection of UHECRs cannot be pursued with techniques measuring directly the particles reaching the Earth from the outer space, due to the diminishing intensity of the flux with increasing energy. What is done is then to take advantage of the so called Extensive Air Shower (EAS), meaning the cascade of particles initiated in the atmosphere by the incoming ultra-high energy cosmic ray. In this section the characteristics of the EAS will be introduced, with the aim of showing how the properties of the primary cosmic-ray can be inferred if some characteristics of the EAS are measured. The components of the EAS (electromagnetic, muonic and hadronic) will be also discussed.

3.1 Extensive air showers

It is convenient to describe the characteristics of the shower in terms of its *longitudinal profile*, defined as the number of particles $N(X)$ as a function of the *slant depth* X (expressed in $\mathrm{g\,cm^{-2}}$ and defined as the column density of air measured from the top of the atmosphere along the direction of the incident primary particle). The slant depth is connected to the vertical altitude h and the distance up the trajectory l, and for small zenith angles θ can be approximated as $l = h/\cos\theta$. The slant depth is therefore connected to those quantities as:

$$X = \int_l^\infty \rho(h(l,\theta))dl \tag{3.1}$$

where ρ is the density of the atmosphere, which in turns depends on temperature and pressure. The vertical slant depth can be expressed as

$$X_\mathrm{v} = X_0 \exp(-h/h_0)\,; \tag{3.2}$$

at the sea level, the vertical atmospheric depth is $X_0 = 1030\ \mathrm{g\,cm^{-2}}$.

The atmosphere can be thought as a calorimeter and the primary energy of the cosmic ray can be determined by considering the energy losses of electrons and positrons (constituting the dominant component of an EAS), due to ionization:

$$(1-F)\,E_0 \sim \alpha \int_0^\infty N(X)\,dX\,, \tag{3.3}$$

where $N(X)$ is the number of charged particles at depth X in the atmosphere, while α is the energy loss per unit path length, being the minimum ionization loss for electrons 2.5 $\mathrm{MeV/g\,cm^{-2}}$, and F is the fraction of energy lost to neutrinos. The muonic component of the shower behaves differently from the electromagnetic one; the number of muons produced in the shower increases as a

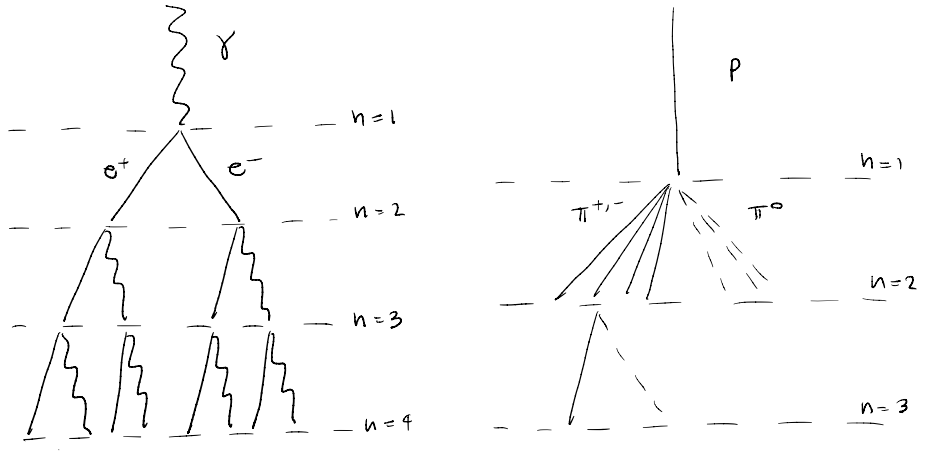

Figure 13: (Handmade) representation of the development of a shower in atmosphere as initiated by a photon (left drawing) and a proton (right drawing).

function of the depth in the atmosphere, reaching a plateau, due to their scarce interactions. On the contrary, electrons and positrons suffer radiative energy losses and pair production, and their number decreases rapidly after reaching a maximum. This is mainly due to the bremsstrahlung losses, that are proportional to $(m_e/M)^2$, where M is the mass of the considered particle. Bremsstrahlung losses for muons are therefore suppressed with respect to electrons, and lose energy by photon-mediated fragmentation of nuclei and by direct pair production. The critical energy (the one at which radiative losses equal the ionization ones) is $E_c^{\mu} \approx 500$ GeV, while the one for electrons is $E_c^{\rm em} \approx 87$ MeV.

The particle densities at the ground, as a function of the distance to the core of the EAS, bring complementary information to the longitudinal profile of the shower, and are treated in the *lateral distribution* of the EAS.

A simple model for the development of electromagnetic cascades was proposed by Heitler [48], and is shown in the left drawing of Fig. 13. The number of particles in the electromagnetic shower at depth X is $N(X) = 2^{X/X_0}$ (being $X_0 = 36.62\ \mathrm{g\,cm^{-2}}$ the electromagnetic radiation length in air), thus the energy of a particle at the same depth is $E(X) = E_0/N(X)$ (being E_0 the energy of the primary photons). The maximum number of particles in the showers is reached at the step where radiative losses equal ionization losses, and is equal to $N(X_{\rm max}) = E_0/E_{\rm c}^{\rm em}$ corresponding to a certain depth in the atmosphere $X_{\rm max}$, which is on average

$$\langle X_{\rm max} \rangle = X_0 \frac{\ln(E_0/E_{\rm c}^{\rm em})}{\ln 2}\,. \tag{3.4}$$

The Heitler model, developed for the electromagnetic showers, can be generalized in order to model also showers initiated by hadrons [49], as depicted in Fig. 13 on the right. After one interaction length, a hadronic particle with energy E_0 produces $n_{\rm tot}$ particles with energy E/n_{tot}; in particular, $(2/3)n_{\rm tot}$ are charged pions while $(1/3)n_{\rm tot}$ are neutral ones, that decay in photons. Charged pions interact until they reach the typical energy for the decay, and therefore decay pro-

ducing one muon per pion. The energy is then shared between the hadronic and electromagnetic part of the shower as:

$$E_{\rm had} = \left(\frac{2}{3}\right)^n E_0, \quad E_{\rm em} = \left[1 - \left(\frac{2}{3}\right)^n\right] E_0 \,. \tag{3.5}$$

Being the electromagnetic component also present in the shower initiated by a hadron, one can easily estimate the maximum number of particles in the shower considering the total multiplicity of hadrons produced in the main interaction, N, and the average hadron energy, E_0/N; the shower maximum of a primary proton is then found by summing the depth of the first interaction of the proton $\lambda_{\rm p}$ and the contribution of the electromagnetic component

$$\langle X^{\rm p}_{\rm max} \rangle \approx \lambda_{\rm p} + X_0 \ln\left(\frac{E_0}{2NE_{\rm c}}\right) \tag{3.6}$$

where the factor 2 takes into account the decay of neutral pions into two photons. This relation also allows to estimate, as reported in Eq. 3.3, the energy of the primary particle from the longitudinal development of the shower. The nuclear composition of the cosmic rays can also be determined on a statistical basis from the longitudinal development of the shower, if the primary nucleus of mass A and energy E is treated as a superposition of A nucleons of energy $E' = E/A$ (*superposition model*, although some more realistic assumptions have to be accounted for, see [50] and references therein). Using the superposition model, the depth at which there is the maximum number of particles in a shower initiated by a nucleus of mass A can be obtained as:

$$\langle X^{\rm A}_{\rm max} \rangle = \langle X^{\rm p}_{\rm max} \rangle - D_{\rm p} \ln A \tag{3.7}$$

where $D_{\rm p}$ is the elongation rate for protons, defined as $D_{\rm p} = {\rm d}\langle X^{\rm p}_{\rm max}\rangle / {\rm d}\ln E = 25 \ {\rm g\,cm^{-2}}$.

The number of muons is strongly connected to the one of charged hadrons, through the number n of generations in the shower. The energy of a pion after the n-th interaction is $E_\pi = E_0/N^n$. The energy continues to split until the stage where the pion reaches the decay energy, $n_{\rm d}$, that corresponds to the depth $\lambda_{\rm d} = c\Gamma\rho\tau$ (Γ is the Lorentz factor of the pion, thus connected to the energy of the primary particle, ρ is the density of the atmosphere and τ is the lifetime of the pion in its rest frame). The decay energy of the pion can be computed as

$$E^\pi_{\rm d} = \frac{E_0}{N^{\rm n_d}} \tag{3.8}$$

and the stage of the shower at which the decay energy is reached is $n_{\rm d} = \ln(E_0/E^\pi_{\rm d})/\ln N$. The total number of muons in a shower is equal to the number of pions with $E_\pi = E^{\rm n_d}_\pi$, and therefore,

$$N_\mu = N_\pi = \left(\frac{2}{3}N\right)^{\rm n_d} \approx \left(\frac{E}{E^\pi_{\rm d}}\right)^\beta \tag{3.9}$$

with $\beta = 1 + \ln\frac{2}{3}N/\ln N$, being $2/3$ the fraction of charged pions. Air shower simulations predict $\beta = 0.88 \div 0.92$, depending on the multiplicity. Because the interaction length drops out in the calculation of $n_{\rm d}$, the number of muons at the ground is expected to be independent of $\lambda_{\rm int}$.

Due to the fact that the transfer of energy to the muons is small, the number of electrons at the shower maximum can be estimated as:

$$N^{\mathrm{p}}_{\mathrm{e,max}} = \frac{E}{E_{\mathrm{c}}^{\mathrm{em}}} - \frac{E_{\mathrm{d}}^{\pi}}{E_{\mathrm{c}}^{\mathrm{em}}} \left(\frac{E}{E_{\mathrm{d}}^{\pi}}\right)^{\beta} \approx \frac{E}{E_{\mathrm{c}}^{\mathrm{em}}} \,. \tag{3.10}$$

Using the superposition model we then find the number of electrons at the shower maximum

$$N^{\mathrm{A}}_{\mathrm{e,max}} \approx A \frac{E}{A E_{\mathrm{c}}^{\mathrm{em}}} = N^{\mathrm{p}}_{\mathrm{e,max}} \tag{3.11}$$

and the number of muons

$$N^{\mathrm{A}}_{\mu,\mathrm{max}} \approx A \left(\frac{E_0/A}{E_{\mathrm{d}}^{\pi}}\right) = N^{\mathrm{p}}_{\mu,\mathrm{max}} A^{1-\beta} \,. \tag{3.12}$$

Therefore, we can conclude that the position in the atmosphere at which the electromagnetic component of the shower reaches its maximum (Eq. 3.7, from the longitudinal profile of the shower) is sensitive to the chemical composition of the primary, as well as the number of muons at the ground (Eq. 3.12, from the lateral distribution of the shower).

Different experimental techniques permit to gather this information from the detection of the EAS. The lateral distribution of the shower, which is then thought to be fundamental in order to deduce the electron-to-muon number and to help in discriminating the mass composition, can be parametrized as done by Greisen [51] and Nishimura and Kamata [52], as

$$\rho_{\mathrm{NGK}}(r,s,N_e) = \frac{N_e}{r_{\mathrm{M}}^2} \frac{\Gamma(4.5-s)}{2\pi\Gamma(s)\Gamma(4.5-2s)} \left(\frac{r}{r_{\mathrm{M}}}\right)^{s-2} \left(1+\frac{r}{r_{\mathrm{M}}}\right)^{s-4.5} \tag{3.13}$$

in terms of the shower age s, the Molière radius r_{M} and the electron shower size N_e. An empirical definition of the age of the shower is [13]:

$$s = \frac{3}{1+2X_{\mathrm{max}}/X} \,; \tag{3.14}$$

simulations show the universality of showers due to the fact that the multiplication and absorption of particles reach equilibrium at the shower maximum [13].

Although the connections between the mass composition and the maximum number of particles in the shower or the particles at the ground are valid, it is not possible to directly measure the mass composition of a shower. What is done is to measure the observables reported in this section and give an interpretation of the mass composition, in terms of hadronic interaction models. Hadronic interactions in air showers are phenomenologically modeled thanks to low-energy experiment data, and are extrapolated at UHE: in fact, at UHE the center of mass energies of the first nucleus-air interactions are beyond accelerator energies. Air shower observables are sensitive to details of the hadronic interactions, such as the multiplicity, the cross section, and the elasticity. Different hadronic interaction models build the observables (such as the average of the maximum number of particles in the shower, the number of muons, etc...) based in different ways on the (extrapolated) details of the interactions. Therefore, the determination of the UHECR mass composition relies on the hadronic model used. A discussion of the effect of uncertainties in hadronic interaction on air shower observables can be found in [53].

3.2 Detection of EASs

To learn about the origin of cosmic rays, the relative abundances of the different nuclei, the distribution in energy of each component and the arrival directions have to be measured. In this section we describe two methods of experimental detection: the particle detector arrays and the fluorescence detection.

Particle detector arrays. The study of UHECRs requires detectors with large areas (hundreds or even thousands of square kilometers) exposed for long periods of time (years). These detectors built on the surface of the Earth are called "air shower arrays" and detect the remnants of the atmospheric cascade of particles initiated by the incident particle. They consist of a set of particle detectors typically arranged in a regular pattern, whose distances change depending of the energy range of interest.

The energy estimate can be done using the measured signal in the detectors, and taking advantage of the fact that showers of any type are expected to have properties similar to a pure electromagnetic cascade, being this generated as possible branch. Fluctuations in the shower size, in particular, are expected to be least near the shower maximum. The method of the Constant Intensity Cuts (CIC) takes advantage of this universality (also discussed in the previous section), extracting the size at maximum that corresponds to a given observed counting rate; this allows then to convert, on average, N_e to $N_{e,max}$. In addition, since the number of particles at maximum is close to the calorimetric measurement of the energy of the primary, this method permits to convert the information on the size to the one on the energy, reducing the dependence on the model. Other methods consist in the use of the density of the shower at some distance from the core, integrating the LDF, which describes the fall-off of signal size with the distance from the shower core. To avoid the inaccuracy due to the assumption of the LDF, Hillas [54] proposed to define the size of the shower using the signal at certain distance; in [55] the optimum distance at which to determine the size of a shower is discussed. Up to the advent of the latest UHECR observatories, this energy estimator has been calibrated with Monte Carlo reference. Nowadays, the calibration is done through the use of hybrid events, as reported in [56].

The nature of the primary cosmic ray can be traced on a statistical basis by comparing the electron-to-muon number ratio, as reported in Sec. 3.1. Furthermore, the arrival time distribution of particles in the surface detectors can be considered. The arrival of the first particles at lateral distance r from the axis is expected to be delayed with respect to a planar shower front. The delay from the longer path length for a particle produced at height h and observed at r can be approximated as [50]:

$$t = \frac{1}{c}(\sqrt{(h^2+r^2)} - h) \propto \frac{r^2}{h}, \; r \ll h\,. \tag{3.15}$$

For $r \ll h$, the delay increases with r but decreases with h thus at a fixed distance r, showers initiated from heavy (light) particles with some energy will be less (more) delayed. Using the time information of signals recorded by the detector, a knowledge of the longitudinal profile of the hadronic component can be obtained. It can be noticed that the muons dominate the early part of the signal in the particle detectors and their corresponding signal is shorter. At the increase of the zenith angle, an early-late time asymmetry can also be observed due to the absorption of the electromagnetic component.

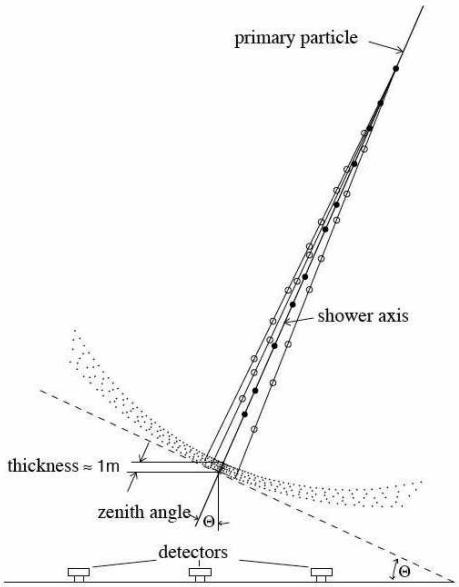

Figure 14: Schematic view of the surface detector reconstruction technique. From Pierre Auger Observatory | Flickr.

The direction of the primary cosmic ray is inferred from the arrival times of signals in at least three non-collinear detectors in an array. In particular, the direction of the shower axis can be determined from the delay of the shower front (as a first approximation considered as planar) reaching different detectors. Fig. 14 shows a schematic view of the surface detectors reconstruction.

Fluorescence detectors. Fluorescence detectors exploit the excitation of nitrogen molecules by particles in the shower and the consequent fluorescence emission of light. The fluorescence detection allows to follow the trajectory of an air shower in the atmosphere and measure the corresponding dissipated energy. The atmosphere acts as a giant calorimeter of more than 10^{10} tons.

The number of emitted photons follows from the ionisation energy deposited from the particles in the shower. The fluorescence light emitted at a certain slant depth X_i is measured at the detector at a time t_i. Given the fluorescence yield Y_i^f at this point of the atmosphere, the number of photons produced at the shower in a slant depth interval ΔX_i is

$$N_\gamma^f(X_i) = Y_i^f \, \omega_i \, \Delta X_i \tag{3.16}$$

where ω_i denotes the energy deposited per unit depth at slant depth X_i, and is defined in [57]. In addition to fluorescence light, also the direct and scattered Cherenkov light hit the photomultiplier and have to be taken into account in the definition of ω_i. Moreover, due to the limited field of view of the fluorescence detector, only a part of the profile is observed. Therefore, a parametrization is used to extrapolate the shower profile outside the observed ranges, as the one proposed by Gaisser and Hillas [58]:

$$N(X) = N_{\max} \left(\frac{X - X_1}{X_{\max} - X_1} \right)^{(X_{\max} - X_1)/\Lambda} \exp\left(- \frac{\mathrm{X} - \mathrm{X}_{\max}}{\Lambda} \right), \tag{3.17}$$

where X_1 and Λ are parameters of the fit. The profile of the shower measured by the fluorescence detector is fundamental to estimate the atmospheric depth of maximum development. The slant

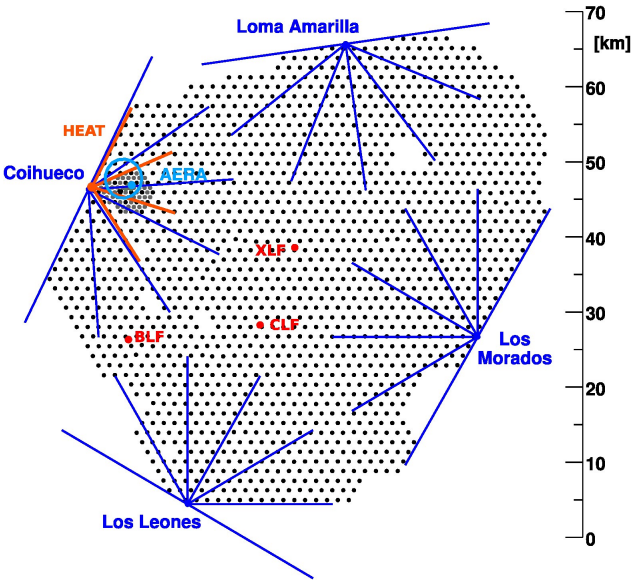

Figure 15: Layout of the Pierre Auger Observatory. Water-Cherenkov detectors are shown as black dots and the azimuthal fields of view of the 27 fluorescence telescopes is indicated by the blue and red lines. The location of the two laser facilities (CLF and XLF) for the monitoring of the aerosol content in the atmosphere are shown with red dots and the area equipped with radio antennas (AERA) is marked with a light-blue circle. From Pierre Auger Observatory | Flickr.

depth position $X_{\rm max}$ at which the maximum of the longitudinal shower profile occurs, together with the width of $X_{\rm max}$ distributions, are very sensitive observables to the composition, as explained in Sec. 3.1. In particular, proton primaries reach the maximum on average deeper in atmosphere with respect to iron nuclei. Furthermore, heavy nuclei are expected to produce shower-to-shower fluctuations smaller than protons.

The direction of the shower with respect to the shower detector plane (plane that includes the location of the telescope and the line of the shower axis) can be determined using the arrival time sequence of the signals at the pixels in the camera (monocular view). The reconstruction can be improved conducting a simultaneous observation from two telescopes.

3.2.1 The Pierre Auger Observatory

The Pierre Auger Observatory [59], located on a vast plain in Argentina, in the Province of Mendoza, at 1440 m above sea level, is the largest observatory to detect cosmic rays ever built and it has been in operation since 2004. It combines Surface Detectors (SD) to measure secondary particles at the ground level together with Fluorescence Detectors (FD) to measure the development of air showers in the atmosphere above the array. This hybrid detection technique combines the calorimetric measurement of the shower energy through fluorescent light with the high-statistics data of the surface array. This technique is similarly exploited by the Telescope Array [60], located in the Northern hemisphere. The properties of the extensive air-showers are, in this way, measured to determine the energy and arrival direction of each cosmic ray and to provide a statistical determination of the distribution of primary masses. Fig. 15 shows the location of the SD stations, the FD sites and the atmospheric monitoring instruments operating at the Observatory.

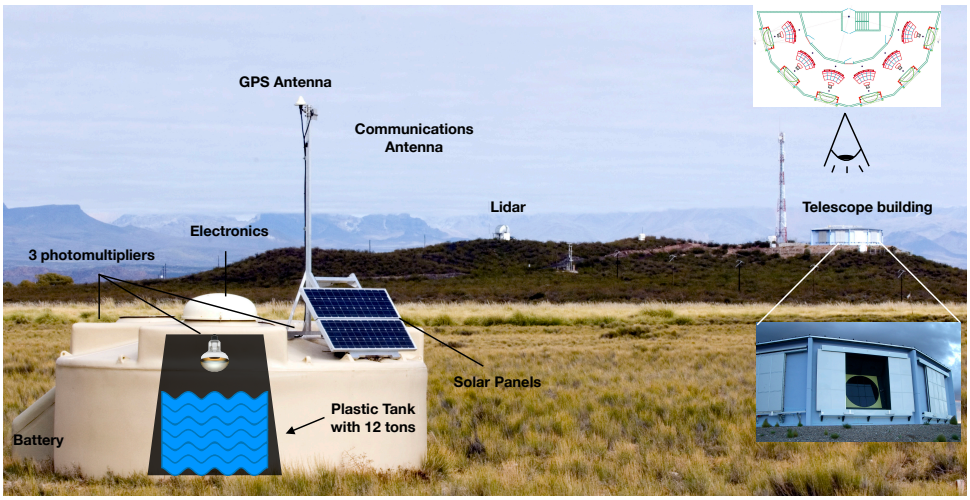

Figure 16: A schematic view of a surface detector station in the field, showing its main components and of a fluorescence building with six fluorescence telescopes. Adapted from Pierre Auger Observatory | Flickr.

The SD array consists of 1600 water-Cherenkov particle detector stations spread over 3000 km^2 on a 1500 m triangular grid. In addition, 61 detectors are distributed over 23.5 km^2 on a 750-m grid (SD-750 or *infill* array). Each water-Cherenkov station is filled with highly-purified water enclosed within a diffusively-reflective liner. The water is viewed from above by three 9-inch photomultiplier tubes (PMTs) in contact with it as shown in Fig. 16. These detect Cherenkov light emitted by charged particles that enter the detectors. The signal measured is expressed in a common calibration unit called vertical equivalent muon (VEM) [61]. The SD array collects EAS at any time with almost 100% duty cycle.

The FD consist of four telescope buildings overlooking the ground array. These are located at Los Leones, Los Morados, Loma Amarilla and Coihueco (see Fig. 15). The data from the fluorescence emission are collected by a set of six telescopes at each of the FD sites, covering 30 degrees of elevation from the ground up and 6 x 30° over the array. Each telescope has a camera with 440 photomultipliers (pixels), recording the ultraviolet light received in each 100 ns time interval as shown in Fig. 16. At each site, an event is recorded and imaged on the camera as a line of activated pixels with a track-like geometrical pattern and a time sequence. Three additional telescopes pointing at higher elevations (HEAT) are located near the Coihueco site to detect lower energy showers. The FD operates during clear moonless nights for a duty cycle of 15%. This setup is complemented by the Auger Engineering Radio Array (AERA) to study radio emission from air showers [56] and by Laser Detection and Ranging (LIDAR) and laser facilities for atmospheric monitoring.

4. Latest results about UHECRs

In this section we briefly report the latest results about UHECRs, mainly summarizing the ones presented by the Pierre Auger Collaboration at the last International Cosmic Ray Conference

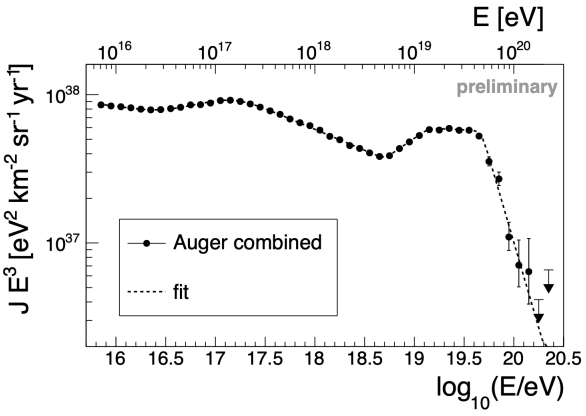

Figure 17: Combined energy spectrum multiplied by E^3, together with the fit function. From [62].

(ICRC)[1].

The energy spectrum is measured with different methods. The ones regarding the SD include the 1500 m array (where both the vertical and the inclined events are taken into account) and the 750 m array. In addition, also the hybrid spectrum and the one obtained from the FD events dominated by Cherenkov light are reported in [62], so that it is possible to provide the spectrum measurement from 6×10^{15} eV, with total exposure of 80000 km^2 sr yr. A combination of these measurements, reported in Fig. 17, is fitted to a function of six power-laws, and some inflection points are shown, thanks to the fit, that were already established: the second knee, the ankle and the suppression. In addition, right above 10^{19} eV, a new inflection is found, called *instep* [41], whose explanation might be connected with propagation effects [63].

The mass composition of the UHECRs can be estimated through the measurement of the atmospheric depth at which the shower reaches the maximum number of particles, $X_{\rm max}$. Independently of the hadronic interaction models, it is found that below the ankle the spread of the masses in the primary cosmic rays is larger than for higher energies [44], as shown in Fig. 18, where the mean and standard deviation of the distributions are reported. These results are also supported by the SD observables sensitive to the mass composition.

In the study of UHECR sources it is fundamental to measure the distribution of the arrival directions of the events, in order to determine the departure from isotropy and the identification of UHECR sources. A dipolar modulation is found, showing amplitude and direction that support the evidence that UHECRs have extragalactic origin [64]; the statistical significance of this large-scale dipolar modulation observed above 8 EeV is increased to 6.6σ in the last update [65], and the dipole directions are reported in Fig. 19. In addition, searches for small and intermediate angular scales are carried out, through correlation analyses with catalogs of candidate extragalactic sources [66].

Multi-messenger studies are possible at the Pierre Auger Observatory. Photon-induced showers can be selected among UHECR events since the $X_{\rm max}$ is expected to be larger and the lateral distribution to be steeper, with the consequence of producing fewer muons than what found in

[1] https://icrc2021.desy.de

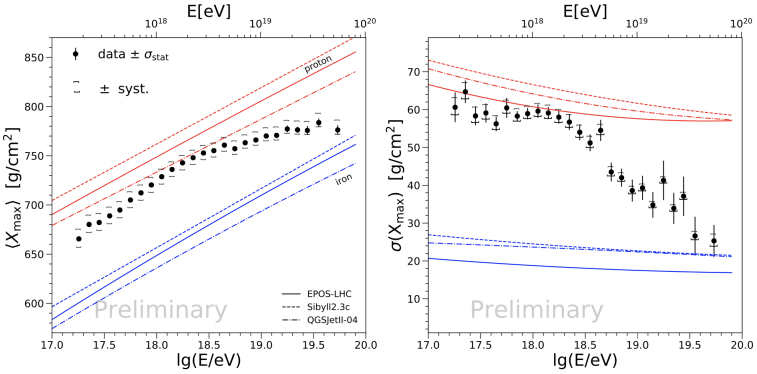

Figure 18: Measurements of $\langle X_{\rm max} \rangle$ (left) and $\sigma(X_{\rm max})$ (right) compared to predictions for proton and iron nuclei of the hadronic models EPOS-LHC, Sibyll 2.3c and QGSJetII-04. From [44].

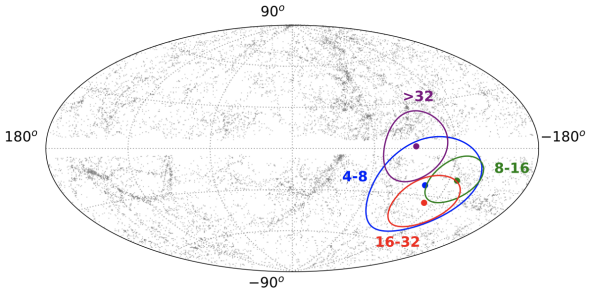

Figure 19: Reconstructed dipole directions in different energy bins and corresponding 68% C.L. uncertainty, in Galactic coordinates. The gray dots indicate the positions of 2MRS galaxies within 100 Mpc. From [65].

hadronic-induced showers. Neutrinos are instead searched for from selections of horizontal showers. Updated limits on photon and neutrino searches are reported in [44]. Follow-up searches for UHE photons from gravitational wave sources are ongoing [67], as well as searches for UHE neutrinos from binary black hole mergers [68].

Due to the extremely high energy carried by UHECRs, it is possible to probe details of particle interactions in showers which would not be accessible at accelerators: a cosmic ray energy of 10^{20} eV corresponds to a center of mass energy of $\sqrt{s} \approx 450$ TeV, which is 30 times the energy achievable at LHC. Discrepancies between the measured number of muons and the expectations from simulations are under study, also through the measurements of the fluctuations of the number of muons in EAS [69].

Several analyses involving the interpretation of data in terms of astrophysical scenarios are developed, such as the one attempting to describe the energy spectrum and mass composition above $10^{17.8}$ eV [70] and the one including also the arrival directions above the ankle [71]. From these analyses, indications towards hard spectral indices and low rigidities of UHECR spectra at the escape from the sources are found.

An upgrade of the Pierre Auger Observatory is well advanced. The surface detection with water-Cherenkov stations is coupled to plastic scintillators (Surface Scintillator Detectors, SSDs) put on top of each detector [72]. This will be used to better discriminate the muonic and electro-

magnetic components of the shower, in order to have a more precise measurement of the nuclear composition of UHECR events.

Acknowledgments. The authors would like to thank J. M. Carmona, A. di Matteo, C. Dobrigkeit, C. Evoli and S. Petrera for comments on the lecture notes.

A. Interaction rate

The expression for the interaction length (Eq. 2.6) can be derived from fundamental quantities of the theory of interactions. We follow here the procedure reported in [13]. We define the particle flux as the rate of particles that cross a plane of surface area dA orthogonal to the particle beam direction

$$\Phi = \frac{dN}{dt\,dA}, \tag{A.1}$$

and the corresponding particle number density $n(\vec{x})$ as

$$n(\vec{x}) = \frac{dN}{d^3x} = \frac{dN}{dl\,dA} = \frac{1}{v}\frac{dN}{dt\,dA} = \frac{1}{\beta c}\Phi, \tag{A.2}$$

where $v = \beta c$ is the particle velocity and $dl = \beta c dt$ is the distance traveled by the particle in the time interval dt. We also introduce the particle flux per unit of energy E and solid angle Ω as

$$\phi(E) = \frac{dN}{dE\,dA\,dt\,d\Omega}. \tag{A.3}$$

Assuming an isotropic distribution for ϕ, the spectral energy density is given by

$$n(E) = \frac{dN}{dE\,d^3x} = \frac{1}{\beta c}\frac{dN}{dE\,dA\,dt} = \frac{4\pi}{\beta c}\phi(E). \tag{A.4}$$

Let us consider a generic process $a + b \to X$, where a is the projectile particle beam, b is the target and X is a generic final state of this interaction process. In the case of a single target particle the interaction rate is given by

$$\frac{dN_{\rm int}}{dt} = \Phi_a \sigma, \tag{A.5}$$

where σ is the cross section of the considered process. Eq. A.5 can be generalized to a distribution of target particles by introducing the number of targets encountered during the time interval dt. This quantity is given by

$$dN_b = n_b \beta c\,dt\,dA = n_b\,dl\,dA = n_b\,dV, \tag{A.6}$$

where n_b is the target number density. Then Eq. A.5 becomes

$$\frac{dN_{\rm int}}{dt\,dV} = n_b \Phi_a \sigma. \tag{A.7}$$

The latter result is valid in the case of interactions between particles with fixed energy. For astrophysical applications we want to take into account a possible particle energy distribution for the

computation of the interaction rate. Considering an isotropic flux of beam particles a with different energies, we obtain that

$$\frac{dN_{\rm int}}{dE_X\,dt\,dV} = 4\pi n_b \int \frac{d\sigma}{dE_X}\phi(E_a)\,dE_a \tag{A.8}$$

$$= n_b \int \frac{d\sigma}{dE_X}\beta_a c n_a(E_a)\,dE_a, \tag{A.9}$$

where $d\sigma/dE_X$ is the differential cross section, and we have used the relation in A.4 for the particle a. In the case of two fluxes of particles with two different energy distributions, we have to introduce the relative velocity between two particles $\beta_{\rm rel}c$ and integrate over both the particle distributions:

$$\frac{dN_{\rm int}}{dE_X\,dt\,dV} = \int \frac{d\sigma}{dE_X}\beta_{\rm rel}c\left(1-\vec{\beta}_a\vec{\beta}_b\right)n_a(E_a)n_b(E_b)\,dE_a\,dE_b. \tag{A.10}$$

Eq. A.10 can be applied to the case of photo-hadronic interactions. When one of the two interacting particles is a photon, we have that $\beta_{\rm rel}=1$ and $\vec{\beta}_a\vec{\beta}_b = \beta_a\cos\theta$, where θ is the angle between the particle momenta in the laboratory frame. In the case of one beam particle with fixed energy, we have that $n_a \propto \delta(E-E_a)$, then the interaction rate becomes

$$\frac{dN_{\rm int}}{dE_X\,dt} = c\int \frac{d\sigma}{dE_X}(1-\beta_a\cos\theta)n_\gamma(\varepsilon)\,d\varepsilon, \tag{A.11}$$

where ε is the photon energy. Since we are interested in the total interaction rate, we have to integrate over dE_X the previous relation:

$$\frac{dN_{\rm int}}{dt} = c\int \sigma(\varepsilon)(1-\beta_a\cos\theta)n_\gamma(\varepsilon)\,d\varepsilon. \tag{A.12}$$

We can redefine the interaction rate by integrating over all the possible initial polarisations of the interaction (i.e. over the angle θ) by assuming an isotropic distribution for the photon field. We then obtain

$$\frac{dN_{\rm int}}{dt} = \frac{c}{4\pi}\int \sigma(\varepsilon)(1-\beta_a\cos\theta)n_\gamma(\varepsilon)\,d\varepsilon\,d\Omega. \tag{A.13}$$

We perform a Lorentz transformation in the reference frame of the particle a. The photon energy ε' is then given by

$$\varepsilon' = \Gamma_a\varepsilon(1-\beta_a\cos\theta), \tag{A.14}$$

$$d\varepsilon' = -\Gamma_a\varepsilon\beta_a\,d\cos\theta, \tag{A.15}$$

where Γ_a is the Lorentz factor of the particle a. Performing the integration over the azimuth angle, we obtain the interaction rate

$$\frac{dN_{\rm int}}{dt} = \frac{c}{2\Gamma_a^2}\int_{\varepsilon'_{\rm th}}^{\infty}\sigma(\varepsilon')\varepsilon'\int_{\varepsilon'/2\Gamma_a}^{\infty}\frac{n_\gamma(\varepsilon)}{\varepsilon^2}\,d\varepsilon\,d\varepsilon'. \tag{A.16}$$

B. Cosmology

Being the CR sources located at cosmological distances, the Robertson-Walker metric describing a homogeneous and isotropic expanding Universe has to be used [73]:

$$ds^2 = dt^2 - c^2R^2(t)\left(\frac{dr^2}{1-kr^2}+r^2(d\theta^2+\sin^2\theta d\phi^2)\right), \tag{B.1}$$

where (t, r, θ, ϕ) are co-moving coordinates; r is dimensionless and $0 \leq r \leq 1$, and the scale factor $R(t)$ has the dimension of length, and given that the universe is spatially homogeneous, it depends only on t. The k parameter can be chosen to be > 0 ($\Omega > 1$), < 0 ($\Omega < 1$) or $= 0$ ($\Omega = 1$) for spaces of constant positive, negative or zero spatial curvature, respectively. In the following, we will always refer to $\Omega = \Omega_m + \Omega_\Lambda$, then $k = 0$ (Ω is here representing the density). The redshift z is thus defined within this metric as

$$1 + z = \frac{R(t_0)}{R(t_1)}, \tag{B.2}$$

meaning the ratio of the detected wavelength to the emitted wavelength of a photon (being R proportional to the wavelength). Thus the conversion between the time and the redshift can be written as

$$\left(\frac{dt}{dz}\right) = -\frac{1}{H_0(1+z)\sqrt{(1+z)^3\Omega_m + \Omega_\Lambda}} = -\frac{\eta(z)}{c}. \tag{B.3}$$

C. Interaction rate and redshift

In order to compute the interaction length of a process at redshift different from zero, how the target photon field appeared in the past has to be known. If we assume that the photon field has been injected in the extragalactic space in the past, the cosmological evolution of its spectral energy density is given by

$$n_\gamma(\varepsilon, z) = (1+z)^2 n_\gamma\left(\frac{\varepsilon}{1+z}\right), \tag{C.1}$$

where $n_\gamma(\varepsilon/(1+z))$ is the spectral energy density at the present time. The factor $(1+z)^2$ comes from the fact that the volume element evolves as $(1+z)^3$, while the energy is redshifted by a factor $(1+z)^{-1}$. Eq. C.1 is valid if there is no feedback from astrophysical sources to the photon field (i.e. the evolution of the field is only driven by the expansion of the Universe). We derive here the evolution of two quantities:

$$n_\gamma = \int d\varepsilon\, n_\gamma(\varepsilon)\,, \quad \rho_\gamma = \int d\varepsilon\, \varepsilon\, n_\gamma(\varepsilon), \tag{C.2}$$

defined as the number density and the energy density of the photon field, respectively. The cosmological evolution of the number density $n_\gamma(z)$ is given by

$$n_\gamma(z) = \int d\varepsilon\, n_\gamma(\varepsilon, z) = (1+z)^2 \int d\varepsilon\, n_\gamma\left(\frac{\varepsilon}{1+z}\right) \tag{C.3}$$

$$= (1+z)^3 \int d\varepsilon\, n_\gamma(\varepsilon) \tag{C.4}$$

$$= (1+z)^3 n_\gamma. \tag{C.5}$$

Similarly, one can show that

$$\rho_\gamma(z) = (1+z)^4 \rho_\gamma. \tag{C.6}$$

Starting from Eq. 2.6, we can define the interaction rate of an UHECR with Lorentz factor Γ at redshift z as

$$\tau^{-1}(\Gamma,z) = \frac{c}{2\Gamma^2}\int_{\varepsilon'_{\rm th}}^{\infty}\sigma(\varepsilon')\varepsilon'\int_{\varepsilon'/2\Gamma}^{\infty}\frac{n_\gamma(\varepsilon,z)}{\varepsilon^2}\,d\varepsilon\,d\varepsilon' \tag{C.7}$$

$$= \frac{c(1+z)^2}{2\Gamma^2}\int_{\varepsilon'_{\rm th}}^{\infty}\sigma(\varepsilon')\varepsilon'\int_{\varepsilon'/2\Gamma}^{\infty}\frac{n_\gamma(\varepsilon/(1+z))}{\varepsilon^2}\,d\varepsilon\,d\varepsilon'. \tag{C.8}$$

We can change the integration variable ε with $\omega(1+z)$; then the interaction rate becomes

$$\tau^{-1}(\Gamma,z) = \frac{c(1+z)}{2\Gamma^2}\int_{\varepsilon'_{\rm th}}^{\infty}\sigma(\varepsilon')\varepsilon'\int_{\varepsilon'/2(1+z)\Gamma}^{\infty}\frac{n_\gamma(\omega)}{\omega^2}\,d\omega\,d\varepsilon' \tag{C.9}$$

$$= \frac{c(1+z)^3}{2((1+z)\Gamma)^2}\int_{\varepsilon'_{\rm th}}^{\infty}\sigma(\varepsilon')\varepsilon'\int_{\varepsilon'/2(1+z)\Gamma}^{\infty}\frac{n_\gamma(\omega)}{\omega^2}\,d\omega\,d\varepsilon' \tag{C.10}$$

$$= (1+z)^3\tau^{-1}((1+z)\Gamma,z=0). \tag{C.11}$$

The interaction length is given by $l=\tau c$ for UHECRs, then the interaction length at redshift z can be written as

$$l(E,z) = \frac{l((1+z)E,z=0)}{(1+z)^3}, \tag{C.12}$$

where we have used the particle energy instead of the particle Lorentz factor.

D. Energy intervals at the epoch of production and observation

In this appendix we derive the connection between energy intervals at the epoch of production and observation of a CR proton, as done in [15, 16]. We define here

$$-\frac{1}{E}\frac{dE}{dt} = \beta_0(E), \tag{D.1}$$

from which we can also define the quantity

$$b_0(E) = -\frac{dE}{dt} = E\beta_0(E), \tag{D.2}$$

where the subscript 0 refers to the fact that these quantities have been defined at redshift $z=0$. We can include the cosmological evolution of the background photon fields by replacing the photon spectral energy density with $n(\varepsilon,t)$. Thus the quantities in Eq. D.1 and D.2 become

$$-\frac{1}{E}\frac{dE}{dt} = \beta(E,t)\ , \quad b(E,t) = E\beta(E,t). \tag{D.3}$$

In the case of a cosmological background photon field, the time variable can be replaced by the redsfhit z. If the photon field evolution is simply given by the expansion of the Universe (i.e. no feedback from astrophysical sources), then $n(\varepsilon,z)$ is related to the density at $z=0$ through

$$n(\varepsilon,z) = (1+z)^3 n((1+z)\varepsilon), \tag{D.4}$$

from which the relations for β and b read

$$\beta(E,z) = (1+z)^3\beta_0((1+z)E), \tag{D.5}$$

$$b(E,z) = (1+z)^2 b_0((1+z)E). \tag{D.6}$$

In order to connect the energy intervals, we want to solve the following energy loss equation

$$\frac{dE_{\rm src}}{dt} = -E_{\rm src}\beta(E_{\rm src}, z(t)), \tag{D.7}$$

where the subscript src refers to the fact that we want to find out the energy at the emission from the source. The β-function is given by the sum of the interaction β-function plus the energy loss due to the expansion of the Universe

$$\beta(E_{\rm src}, z(t)) \;\; \rightarrow \;\; \beta(E_{\rm src}, z(t)) + H(z(t)), \tag{D.8}$$

where $H(z(t))$ is the Hubble parameter at the time t. Given the initial condition $E(t=t_0) = E$, where $t = t_0$ is the present time, the solution of Eq. D.7 for a generic time $t < t_0$ is

$$E_{\rm src}(t) = E + \int_t^{t_0} d\tau E_{\rm src}(\tau) H(z(\tau)) + \int_t^{t_0} d\tau E_{\rm src}(\tau)\beta(E_{\rm src}(\tau), z(\tau)). \tag{D.9}$$

We can write this solution using the redshift parameter such that $z(t=t_0) = 0$. The energy loss equation for protons in redshift reads

$$E_{\rm src}(z) = E + \int_0^z d\omega \frac{E_{\rm src}(\omega)}{1+\omega} + \int_0^z d\omega \frac{E_{\rm src}(\omega)\beta(E_{\rm src}(\omega),\omega)}{H(\omega)(1+\omega)}. \tag{D.10}$$

The relations D.2 and D.5 can be used to show that

$$\beta(E,z) = (1+z)^3\beta_0((1+z)E) = \frac{(1+z)^2}{E} b_0((1+z)E), \tag{D.11}$$

and therefore

$$E_{\rm src}(z) = E + \int_0^z d\omega \frac{E_{\rm src}(\omega)}{1+\omega} + \int_0^z d\omega \frac{1+\omega}{H(\omega)} b_0((1+\omega)E_{\rm src}(\omega)). \tag{D.12}$$

If the previous equation is differentiated with respect to E_0, the expansion factor of the energy interval can be computed as

$$\begin{aligned} y(z) &= 1 + \int_0^z d\omega \frac{y(\omega)}{1+\omega} + \int_0^z d\omega \frac{1+\omega}{H(\omega)} \frac{db_0((1+\omega)E_{\rm src}(\omega))}{dE} \\ &= 1 + \int_0^z d\omega \frac{y(\omega)}{1+\omega} + \int_0^z d\omega \frac{(1+\omega)^2}{H(\omega)} \frac{db_0((1+\omega)E_{\rm src}(\omega))}{d((1+\omega)E_{\rm src}(\omega))} y(\omega), \end{aligned} \tag{D.13}$$

whose corresponding differential equation is

$$\frac{1}{y}\frac{dy}{dz} = \frac{1}{1+z} + \frac{(1+z)^2}{H(z)} \frac{db((1+z)E_{\rm src}(z))}{d((1+z)E_{\rm src}(z))}. \tag{D.14}$$

The solution of Eq. D.14 is the connection between the energy intervals:

$$y(z) = (1+z)\exp\left[\frac{1}{H_0}\int_0^z d\omega \frac{(1+\omega)^2}{\sqrt{(1+\omega)^3\Omega_m + \Omega_\Lambda}} \frac{db_0((1+\omega)E_{\rm src}(\omega))}{d((1+\omega)E_{\rm src}(\omega))}\right], \tag{D.15}$$

which therefore enters in the computation of the expected number of particles at Earth. For the corresponding semi-analytical computation of the flux at Earth from UHECR nuclei, see [12, 25].

References

[1] C. Evoli, https://doi.org/10.5281/zenodo.4396125, Zenodo, 2021

[2] D. Pacini, Nuovo Cim. **8** (1912), 93-100 doi:10.1007/BF02957440 [arXiv:1002.1810 [physics.hist-ph]].

[3] V. F. Hess, Phys. Z. **13** (1912), 1084-1091

[4] P. O. Lagage and C. J. Cesarsky, Astron. Astrophys. **125** (1983), 249-257

[5] L. O. Drury, Rept. Prog. Phys. **46** (1983), 973-1027 doi:10.1088/0034-4885/46/8/002

[6] A. M. Hillas, Ann. Rev. Astron. Astrophys. **22** (1984), 425-444 doi:10.1146/annurev.aa.22.090184.002233

[7] R. Alves Batista, J. Biteau, M. Bustamante, K. Dolag, R. Engel, K. Fang, K. H. Kampert, D. Kostunin, M. Mostafa and K. Murase, *et al.* Front. Astron. Space Sci. **6** (2019), 23 doi:10.3389/fspas.2019.00023 [arXiv:1903.06714 [astro-ph.HE]].

[8] N. Globus, D. Allard and E. Parizot, Astron. Astrophys. **479** (2008), 97 doi:10.1051/0004-6361:20078653 [arXiv:0709.1541 [astro-ph]].

[9] S. Hackstein, F. Vazza, M. Brüggen, J. G. Sorce and S. Gottlöber, Mon. Not. Roy. Astron. Soc. **475** (2018) no.2, 2519-2529 doi:10.1093/mnras/stx3354 [arXiv:1710.01353 [astro-ph.CO]].

[10] K. Greisen, Phys. Rev. Lett. **16** (1966), 748-750 doi:10.1103/PhysRevLett.16.748

[11] G. T. Zatsepin and V. A. Kuzmin, JETP Lett. **4** (1966), 78-80

[12] R. Aloisio, V. Berezinsky and S. Grigorieva, Astropart. Phys. **41** (2013), 73-93 doi:10.1016/j.astropartphys.2012.07.010 [arXiv:0802.4452 [astro-ph]].

[13] T. K. Gaisser, R. Engel and E. Resconi, "Cosmic Rays and Particle Physics. Second Edition," Cambridge, 2016

[14] D. Boncioli, "Study of extragalactic propagation of cosmic rays. Applications to Pierre Auger Observatory data," PhD Thesis, University of Roma Tor Vergata, December 2011.

[15] V. Berezinsky, A. Z. Gazizov and S. I. Grigorieva, Phys. Rev. D **74** (2006), 043005 doi:10.1103/PhysRevD.74.043005 [arXiv:hep-ph/0204357 [hep-ph]].

[16] V. S. Berezinsky and S. I. Grigor'eva, Astron. Astrophys. **199** (1988), 1-12

[17] V. Berezinsky, A. Z. Gazizov and S. I. Grigorieva, Phys. Lett. B **612** (2005), 147-153 doi:10.1016/j.physletb.2005.02.058 [arXiv:astro-ph/0502550 [astro-ph]].

[18] J. Heinze, D. Boncioli, M. Bustamante and W. Winter, Astrophys. J. **825** (2016) no.2, 122 doi:10.3847/0004-637X/825/2/122 [arXiv:1512.05988 [astro-ph.HE]].

[19] A. M. Hopkins and J. F. Beacom, Astrophys. J. **651** (2006), 142-154 doi:10.1086/506610 [arXiv:astro-ph/0601463 [astro-ph]].

[20] A. Aab *et al.* [Pierre Auger], Phys. Rev. D **90** (2014) no.12, 122005 doi:10.1103/PhysRevD.90.122005 [arXiv:1409.4809 [astro-ph.HE]].

[21] A. Aab *et al.* [Pierre Auger], Phys. Rev. D **90** (2014) no.12, 122006 doi:10.1103/PhysRevD.90.122006 [arXiv:1409.5083 [astro-ph.HE]].

[22] J. L. Puget, F. W. Stecker and J. H. Bredekamp, Astrophys. J. **205** (1976), 638-654 doi:10.1086/154321

[23] L. Morejon, A. Fedynitch, D. Boncioli, D. Biehl and W. Winter, JCAP **11** (2019), 007 doi:10.1088/1475-7516/2019/11/007 [arXiv:1904.07999 [astro-ph.HE]].

[24] D. Biehl, D. Boncioli, A. Fedynitch and W. Winter, Astron. Astrophys. **611** (2018), A101 doi:10.1051/0004-6361/201731337 [arXiv:1705.08909 [astro-ph.HE]].

[25] R. Aloisio, V. Berezinsky and S. Grigorieva, Astropart. Phys. **41** (2013), 94-107 doi:10.1016/j.astropartphys.2012.06.003 [arXiv:1006.2484 [astro-ph.CO]].

[26] R. Alves Batista, A. Dundovic, M. Erdmann, K. H. Kampert, D. Kuempel, G. Müller, G. Sigl, A. van Vliet, D. Walz and T. Winchen, JCAP **05** (2016), 038 doi:10.1088/1475-7516/2016/05/038 [arXiv:1603.07142 [astro-ph.IM]].

[27] R. Aloisio, D. Boncioli, A. Di Matteo, A. F. Grillo, S. Petrera and F. Salamida, JCAP **11** (2017), 009 doi:10.1088/1475-7516/2017/11/009 [arXiv:1705.03729 [astro-ph.HE]].

[28] A. di Matteo, "Ultra-high-energy cosmic ray phenomenology: Monte Carlo simulations and experimental data," PhD Thesis, University of L'Aquila, 2016.

[29] R. Alves Batista, D. Boncioli, A. di Matteo, A. van Vliet and D. Walz, JCAP **10** (2015), 063 doi:10.1088/1475-7516/2015/10/063 [arXiv:1508.01824 [astro-ph.HE]].

[30] A. Aab *et al.* [Pierre Auger], JCAP **04** (2017), 038 [erratum: JCAP **03** (2018), E02] doi:10.1088/1475-7516/2017/04/038 [arXiv:1612.07155 [astro-ph.HE]].

[31] R. Engel, D. Seckel and T. Stanev, Phys. Rev. D **64** (2001), 093010 doi:10.1103/PhysRevD.64.093010 [arXiv:astro-ph/0101216 [astro-ph]].

[32] R. Aloisio, D. Boncioli, A. di Matteo, A. F. Grillo, S. Petrera and F. Salamida, JCAP **10** (2015), 006 doi:10.1088/1475-7516/2015/10/006 [arXiv:1505.04020 [astro-ph.HE]].

[33] G. B. Gelmini, O. Kalashev and D. V. Semikoz, JCAP **01** (2012), 044 doi:10.1088/1475-7516/2012/01/044 [arXiv:1107.1672 [astro-ph.CO]].

[34] T. Abu-Zayyad *et al.* [Telescope Array], Astropart. Phys. **61** (2015), 93-101 doi:10.1016/j.astropartphys.2014.05.002 [arXiv:1305.7273 [astro-ph.HE]].

[35] A. Aab *et al.* [Pierre Auger], [arXiv:1307.5059 [astro-ph.HE]].

[36] A. Aab *et al.* [Pierre Auger], JCAP **10** (2019), 022 doi:10.1088/1475-7516/2019/10/022 [arXiv:1906.07422 [astro-ph.HE]].

[37] J. Heinze, A. Fedynitch, D. Boncioli and W. Winter, Astrophys. J. **873** (2019) no.1, 88 doi:10.3847/1538-4357/ab05ce [arXiv:1901.03338 [astro-ph.HE]].

[38] R. Alves Batista, R. M. de Almeida, B. Lago and K. Kotera, JCAP **01** (2019), 002 doi:10.1088/1475-7516/2019/01/002 [arXiv:1806.10879 [astro-ph.HE]].

[39] A. De Angelis, G. Galanti and M. Roncadelli, Mon. Not. Roy. Astron. Soc. **432** (2013), 3245-3249 doi:10.1093/mnras/stt684 [arXiv:1302.6460 [astro-ph.HE]].

[40] R. Aloisio, P. Blasi, P. L. Ghia and A. F. Grillo, Phys. Rev. D **62** (2000), 053010 doi:10.1103/PhysRevD.62.053010 [arXiv:astro-ph/0001258 [astro-ph]].

[41] A. Aab *et al.* [Pierre Auger], Phys. Rev. D **102** (2020) no.6, 062005 doi:10.1103/PhysRevD.102.062005 [arXiv:2008.06486 [astro-ph.HE]].

[42] D. Boncioli, A. di Matteo, F. Salamida, R. Aloisio, P. Blasi, P. L. Ghia, A. Grillo, S. Petrera and T. Pierog, PoS **ICRC2015** (2016), 521 doi:10.22323/1.236.0521 [arXiv:1509.01046 [astro-ph.HE]].

[43] D. Boncioli [Pierre Auger], PoS **ICRC2017** (2018), 561 doi:10.22323/1.301.0561

[44] A. Aab *et al.* [Pierre Auger], [arXiv:1909.09073 [astro-ph.HE]].

[45] P. Abreu *et al.* [Pierre Auger], JCAP **01** (2022) no.01, 023 doi:10.1088/1475-7516/2022/01/023 [arXiv:2112.06773 [astro-ph.HE]].

[46] A. Addazi, J. Alvarez-Muniz, R. A. Batista, G. Amelino-Camelia, V. Antonelli, M. Arzano, M. Asorey, J. L. Atteia, S. Bahamonde and F. Bajardi, *et al.* [arXiv:2111.05659 [hep-ph]].

[47] R. Engel, D. Heck and T. Pierog, Ann. Rev. Nucl. Part. Sci. **61** (2011), 467-489 doi:10.1146/annurev.nucl.012809.104544

[48] W. Heitler, "The Quantum Theory of Radiation", third edition, Oxford University Press, London, 1954

[49] J. Matthews, Astropart. Phys. **22** (2005), 387-397 doi:10.1016/j.astropartphys.2004.09.003

[50] K. H. Kampert and M. Unger, Astropart. Phys. **35** (2012), 660-678 doi:10.1016/j.astropartphys.2012.02.004 [arXiv:1201.0018 [astro-ph.HE]].

[51] K. Greisen, Ann. Rev. Nucl. Part. Sci. **10** (1960), 63-108 doi:10.1146/annurev.ns.10.120160.000431

[52] K. Kamata and J. Nishimura, Prog. Theoret. Phys. Suppl. 6 (1958) 93

[53] R. Ulrich, R. Engel and M. Unger, Phys. Rev. D **83** (2011), 054026 doi:10.1103/PhysRevD.83.054026 [arXiv:1010.4310 [hep-ph]].

[54] A. M. Hillas, Acta Phys. Acad. Sci. Hung. **29** (1970), Suppl. 3, 355

[55] D. Newton, J. Knapp and A. A. Watson, Astropart. Phys. **26** (2007), 414-419 doi:10.1016/j.astropartphys.2006.08.003 [arXiv:astro-ph/0608118 [astro-ph]].

[56] A. Aab *et al.* [Pierre Auger], Nucl. Instrum. Meth. A **798** (2015), 172-213 doi:10.1016/j.nima.2015.06.058 [arXiv:1502.01323 [astro-ph.IM]].

[57] M. Unger, B. R. Dawson, R. Engel, F. Schussler and R. Ulrich, Nucl. Instrum. Meth. A **588** (2008), 433-441 doi:10.1016/j.nima.2008.01.100 [arXiv:0801.4309 [astro-ph]].

[58] T.K Gaisser and A.M. Hillas, Proc. of 15th Int. Cosmic Ray Conf., Plovdiv 8 (1977) 353–357

[59] A. Aab *et al.* [Pierre Auger], Nucl. Instrum. Meth. A **798** (2015) 172-213 , doi:10.1016/j.nima.2015.06.058

[60] T. Abu-Zayyad *et al.* [Telescope Array], Nucl. Instrum. Meth. A **689** (2013), 87-97 doi:10.1016/j.nima.2012.05.079 [arXiv:1201.4964 [astro-ph.IM]].

[61] J. Abraham *et al.* [Pierre Auger], Nucl. Instrum. Meth. A, **613** (2010), no.1, 29-39, doi:10.1016/j.nima.2009.11.018

[62] V. Novotny [Pierre Auger], PoS **ICRC2021** (2021), 324

[63] A. Aab *et al.* [Pierre Auger], Phys. Rev. Lett. **125** (2020) no.12, 121106 doi:10.1103/PhysRevLett.125.121106 [arXiv:2008.06488 [astro-ph.HE]].

[64] A. Aab *et al.* [Pierre Auger], Science **357** (2017) no.6537, 1266-1270 doi:10.1126/science.aan4338 [arXiv:1709.07321 [astro-ph.HE]].

[65] R. Menezes [Pierre Auger] PoS **ICRC2021** (2021), 335

[66] J. Biteau [Pierre Auger], PoS **ICRC2021** (2021), 307

[67] P. Ruehl [Pierre Auger], PoS **ICRC2021** (2021), 973

[68] M. Schimp [Pierre Auger], PoS **ICRC2021** (2021), 968

[69] A. Aab *et al.* [Pierre Auger], Phys. Rev. Lett. **126** (2021) no.15, 152002 doi:10.1103/PhysRevLett.126.152002 [arXiv:2102.07797 [hep-ex]].

[70] E. Guido [Pierre Auger], PoS **ICRC2021** (2021), 311

[71] T. Bister [Pierre Auger], PoS **ICRC2021** (2021), 368

[72] G. Cataldi [Pierre Auger], PoS **ICRC2021** (2021), 251

[73] E. W. Kolb and M. S. Turner, "The Early Universe," Westview, 1994